

# Dust grain dynamics in C-Type shock waves in molecular clouds

J. F. Chapman<sup>1,2\*</sup> and Mark Wardle<sup>2†</sup>

<sup>1</sup> School of Physics, University of Sydney, NSW 2006, Australia

<sup>2</sup> Department of Physics, Macquarie University, Sydney, NSW 2109, Australia

Submitted to MNRAS 29 July 2005

## ABSTRACT

We investigate the role and behaviour of dust grains in C-type MHD shock waves in weakly ionized, dense molecular clouds. The structure of C-type shocks is largely determined by the coupling of the charged species and the magnetic field. In weakly ionized clouds, charged dust grains enhance the energy and momentum transfer between the magnetic field and the neutral fluid, and dominate the neutral collisional heating rate. New shock models are developed here for steady oblique C-type shock structures with shock speed  $v_s = 18\text{km/s}$ , pre-shock number density  $n_H = 10^5\text{cm}^{-3}$ , and a grain population represented by either a single grain species or a MRN grain size distribution. The grain size distribution is calculated using Gauss-Legendre weights and the integrals over the continuous distribution of grain sizes are converted to a series of separate grain bins or ‘size classes’. The dynamics of each grain size class various through the shock front; smaller grains remain coupled to the magnetic field and larger grains are partially decoupled from the magnetic field due to collisions with the neutrals. The charges on the grains are allowed to vary, via the sticking and re-releasing of electrons, increasing with increasing electron temperature. The increase in grain charge increases the coupling of the grains to the magnetic field, and magnetic field rotation out of the shock plane is suppressed. MRN(mantles) and MRN(PAHs) distributions are also compared with the standard MRN model. Increasing the grain sizes in the MRN(mantles) model leads to an increase in the collisional heating of the neutrals leading to hotter, thinner shock structures than those using a standard MRN distribution. With the addition of PAHs, the electron abundance is reduced and the grain charge is held constant, resulting in less grain coupling to the magnetic field, and substantial rotation of the magnetic field out of the shock plane. The effects of varying the orientation of the pre-shock magnetic field  $\mathbf{B}_0$  with the shock normal, specified by the angle  $\theta$ , are also considered. It is found that there are critical values of  $\theta$  below which the shock is no longer C-type and the transition becomes C\* or J-type. The degree of non-coplanarity of the shock solution depends upon the grain model chosen, as well as the angle  $\theta$ .

**Key words:** MHD - waves - ISM: clouds - dust extinction - ISM: magnetic fields

## 1 INTRODUCTION

Interstellar shock waves play an integral part in the chemical and physical evolution of the interstellar medium. They are driven by cloud-cloud collisions, stellar winds and supernova explosions (e.g. McCray & Snow 1979). They cause large increases in the local pressure leading to both compression and heating of the gas. As a result, the local increase in density

leads to an increase in the rates at which chemical reactions can occur. C-type shocks may be associated with strong infrared emission lines (Draine et al. 1983), and shock models have been used to explain lines in the K-L region of Orion (Draine & Roberge 1982; Chernoff, McKee & Hollenbach 1982). C-type shocks may also be responsible for the absorption lines along lines of sight, in particular of CH+, in diffuse clouds (Flower, Pineau des Forets & Hartquist 1985; Draine & Katz 1986a,b; Pineau des Forets et al. 1986).

The nature and structure of shock waves travelling through molecular clouds are strongly dependent upon the

\* E-mail: jchapman@physics.mq.edu.au

† E-mail: wardle@physics.mq.edu.au

strength of the ambient magnetic field  $\mathbf{B}_0$  as well as the local ionization fraction. When the magnetic field strength is large and fractional ionization low, a multifluid magnetohydrodynamic (MHD) description of the fluid is usually required (Mullan 1971). In the multifluid treatment, there are two speeds at which compressive disturbances may propagate. In the charged component of the medium, disturbances can propagate at the fast magnetosonic speed which is dependent upon both the magnitude  $|B_0|$  and the orientation of  $\mathbf{B}_0$  with the local shock normal. In the neutral fluid, compressive disturbances propagate at the neutral sound speed.

The charged fluids gain energy and momentum from the magnetic field  $\mathbf{B}$ , and are coupled to the neutral fluid via collisions, transferring energy and momentum, acting to weakly couple the neutrals to  $\mathbf{B}$ . If the fractional ionization rate is small enough, leading to a low neutral-ion collision rate, the two fluids can be thought of as separate and interpenetrating fluids (Draine 1980; Draine et al. 1983). The ions and electrons contribute only small amounts of mass and pressure, however the magnetic fields are strong enough to influence the shock dynamics. If the shock speed is less than the (fast) magnetosonic speeds of the charged fluids, the charged species are accelerated ahead of the neutrals, via ambipolar diffusion in a magnetic precursor (Draine 1980). If the neutral temperature remains low enough inside the shock and the neutral flow is everywhere supersonic, the shock is C-type and all the hydrodynamic variables remain continuous.

At low enough densities, a three fluid system is adequate with the inclusion of neutrals, ions and electrons. The grains may be ignored since their contribution to the energy and momentum of the neutrals is negligible. For densities  $n_H \gtrsim 10^2 \text{ cm}^{-3}$  the energy and momentum transferred from the charged dust grains to the neutrals can no longer be neglected (e.g., Draine et al. 1983), and in regions of high density,  $n_H \sim 10^5 \text{ cm}^{-3}$ , and the grains dominate the collisional heating of the neutrals. The grain abundances in the interstellar medium obey a size distribution (e.g., Mathis, Rumpl & Nordsieck 1977; Draine & Lee 1984; Weingartner & Draine 2001), and for large grain sizes the friction between the grains and neutrals can become great enough that the grains are decoupled from  $\mathbf{B}$ . In the opposite limit, smaller grains may remain tied to  $\mathbf{B}$ . Dust grains also have the potential to drift with respect to the neutral fluid and move out of the shock plane, since grain-neutral collisions can cause their partial decoupling from  $\mathbf{B}$  leading to non-coplanar shock structures.

For perpendicular shocks with  $\mathbf{B}_0$  oriented perpendicular to the local shock normal  $\hat{\mathbf{n}}$ , changes in  $\mathbf{B}$  and the dynamic variables inside the shock are restricted to the shock plane containing  $\mathbf{B}_0$  and  $\hat{\mathbf{n}}$  (e.g., Draine et al. 1983; Flower & Pineau des Forêts 2003). When  $\mathbf{B}_0$  is oriented obliquely with the shock normal, there is a current parallel to the  $\mathbf{B}$  component transverse to the shock propagation direction.  $\mathbf{B}_{\perp}$ , the  $\mathbf{B}$  component perpendicular to  $\hat{\mathbf{n}}$ , can rotate out of the shock plane inside the shock before returning to the shock plane downstream. Wardle & Draine (1987) demonstrated that by changing only the transverse component of  $\mathbf{B}$ , very different hydrodynamic shock structures are found.

Pilipp & Harquist (1994) investigated the rotation of  $\mathbf{B}$  in fast steady shock structures with the inclusion of one grain

species. This involved integration of the shock fluid conservation equations from upstream to downstream which proved difficult for shock speeds  $\gtrsim 3 \text{ km s}^{-1}$ . Pilipp & Harquist (1994) concluded that steady fast shock solutions do not exist for these conditions. Wardle (1998) showed that these solutions were in fact intermediate, not fast, solutions which do not exist for shock speeds above a critical value. Wardle (1998) presented magnetic field ( $B_x$  versus  $B_y$ ) phase space topologies, demonstrating that the shock solution belongs to a one-parameter family. Integration from upstream becomes complicated since the phase space trajectories can diverge due to finite numerical precision, and end up on neighbouring intermediate solutions which can become unphysical. Integrating from the downstream state ensures that the correct fast solution trajectory is followed.

In this paper we investigate the non-coplanar nature of C-type shocks with the inclusion of a grain size distribution. The shock is assumed steady state since the time scales over which the fluid variables vary are longer than the time required to transverse the shock. The methodology of Wardle (1998) is extended to include a grain size distribution and the integration of the energy equation allows for radiative cooling. The shock problem comprises of three ordinary differential equations (ODEs) in  $B_x$ ,  $B_y$ , and pressure  $P$ , along with algebraic expressions for the neutral velocity components, electric field components, and charged species properties. It is a two point boundary problem connecting the upstream and downstream states, and integration proceeds from downstream to upstream to ensure the fast shock solution. With radiative cooling the fluids do not cool to their final temperature until far downstream of the shock front, and integration over such long time scales is infeasible (e.g., Draine 1980). A shooting integration method is implemented which searches for an initial state inside the cooling zone which, after integration towards upstream, yields the pre-shock state. Conditions inside molecular clouds are assumed,  $n_H = 10^5 \text{ cm}^{-3}$ , with shock speed  $v_s \sim 18 \text{ km s}^{-1}$ .

The derivation of the governing shock equations are given in Section 2, the shock jump conditions are derived in Section 3, and the heating and cooling processes are discussed in Section 4. The treatment of the charged species are addressed in Section 5, along with the derivation for both the electron and grain Hall parameters and the electric field component  $E'_z$ , in Sections 6 and 7, respectively. The shock calculation and integration methods are explained in Section 8 followed by the results in Section 9. A discussion and summary are presented in Sections 10 and 11.

## 2 FLUID EQUATIONS

The fluid is weakly ionized, and the inertia and thermal pressures of the charged species are neglected, as well as most processes that create and destroy species. There is only the one exception, when grain charging is used (equation (56)) the electrons are allowed to stick to the grains, and so electrons are removed from, or injected into, the electron fluid to conserve charge density (equation (24)). Each species is characterized by a mass  $m$ , mass and number densities  $\rho$  and  $n$ , respectively, charge  $Ze$  and velocity  $\mathbf{v}$ . Charged species are given a subscript of either  $e$ ,  $i$  or  $g$ , denoting electrons, ions and grains, respectively. A subscript of  $j$  represents

any charged species. The pre-shock medium has mass and number densities  $\rho_0$  and  $n_0$ , respectively, magnetic field  $\mathbf{B}_0$ , pressure  $P_0$ , temperature  $T_0$  and the incoming fluid has a speed  $v_s$ . The shock is assumed steady and plane-parallel  $\partial/\partial t = \partial/\partial x = \partial/\partial y = 0$  and the coordinate system is defined in the shock frame with  $\mathbf{B}_0$  lying in the  $x - z$  plane making an angle  $\theta$  with the  $z$  axis. The incoming flow is parallel to the  $z$  axis. The equations for a steady multifluid flow are then given by the conservation of mass

$$\frac{d\rho v_z}{dz} = 0, \quad (1)$$

momentum

$$\rho v_z \frac{d\mathbf{v}}{dz} + P \frac{d\mathbf{v}}{dz} \hat{\mathbf{z}} = \frac{\mathbf{J} \times \mathbf{B}}{c}, \quad (2)$$

and energy

$$\frac{d(Uv_z)}{dz} + P \frac{dv_z}{dz} = G - \Lambda, \quad (3)$$

along with the following from Maxwell's equations:

$$\frac{dE_{x,y}}{dz} = 0 \quad (4)$$

and

$$\frac{dB_z}{dz} = 0. \quad (5)$$

Lastly, from Ampere's law:

$$\frac{dB_x}{dz} = \frac{4\pi}{c} J_y, \quad (6)$$

$$\frac{dB_y}{dz} = -\frac{4\pi}{c} J_x \quad (7)$$

and

$$J_z = 0. \quad (8)$$

$P$  and  $U$  denote the neutral thermal pressure and internal energy,  $G$  and  $\Lambda$ , the heating and cooling rates per unit volume respectively, and  $\mathbf{E}$ ,  $\mathbf{B}$  and  $\mathbf{J}$  are the electric field, magnetic field, and current density, respectively, with

$$P = \frac{\rho k T}{m}. \quad (9)$$

The internal energy  $U$  is the sum of the thermal kinetic energy and excitation energy of the excited molecules

$$U = \left( \frac{3}{2} + \sum_l p_l \frac{E_l}{kT} \right) P \quad (10)$$

where the summation is over the electronic, rotational and vibrational levels  $l$ , with corresponding probabilities  $p_l$  and energy  $E_l$ . In a  $H_2$  gas the vibrationally excited levels have negligible populations, and the rotational levels have a thermalized distribution, and the sum can be taken as unity (Wardle 1991; Hartquist & Caselli 1998) which is a good approximation in the hottest part of the shock where the pressure becomes important. Equation (10) becomes

$$U = \frac{P}{\gamma - 1}. \quad (11)$$

where  $\gamma$  is the adiabatic index with  $\gamma = 7/5$ .

From mass conservation of the charged species

$$\frac{d}{dz} (\rho_j v_{zj}) = 0. \quad (12)$$

The current density is given by

$$\mathbf{J} = e \sum_j n_j Z_j \mathbf{v}_j, = e \sum_j n_j Z_j (\mathbf{v}_j - \mathbf{v}), \quad (13)$$

assuming charge neutrality

$$\sum_j Z_j n_j = 0. \quad (14)$$

$(\mathbf{v}_j - \mathbf{v})$  is the drift velocity of a species  $j$  with respect to the neutrals. The grains obey a continuous size distribution implying equation (14) contains an integral over grain size. However, the MRN size distribution is calculated using Gauss-Legendre weights (Section 5.2), and the distribution is represented by a series of discrete grain size bins each with a specified number density and charge. Each grain bin is then considered a separate species  $j$  in equation (13).

The rotation of  $\mathbf{B}_\perp (|\mathbf{B}_\perp| = \sqrt{B_x^2 + B_y^2})$  inside the shock front is driven by the Hall current along the  $\mathbf{E}' \times \mathbf{B}$  direction, and the Pedersen current along the  $\mathbf{E}'$  direction. The difference in drift speeds between charged species drives the Hall current. In the ambipolar diffusion limit all charged species are highly coupled to  $\mathbf{B}$  and the Hall current vanishes. In this limit the magnetic forces on the charged species dominates the neutral collisional drag which is the case for the electrons and ions in molecular clouds. When charged dust grains are present the neutral-grain drag force is non-negligible resulting in a non-zero Hall current and there is rotation of  $\mathbf{B}_\perp$ . Wardle & Ng (1999) demonstrated that for dense molecular gas, the contribution of dust grains to the Hall conductivity leads to substantial changes in the dynamics of the gas as well as the evolution of  $\mathbf{B}$ .

Treating the charged particles as test particles, and neglecting their inertia, their drift through the neutrals is

$$n_j Z_j e \left( \mathbf{E} + \frac{\mathbf{v}_j}{c} \times \mathbf{B} \right) + \gamma_j \rho_j \rho (\mathbf{v} - \mathbf{v}_j) = 0, \quad (15)$$

which represents the balance between the electromagnetic forces and the collisional drag (Draine 1980; Shu 1983). The rate coefficient for elastic scattering between particles of a species  $j$  and the neutrals,  $\langle \sigma v \rangle_j$ , is related to  $\gamma_j$  via

$$\gamma_j = \frac{\langle \sigma v \rangle_j}{m_j + m}. \quad (16)$$

If  $\sigma$  is not a function of  $v$ ,  $\langle \sigma v \rangle_j$  may be written as  $\sigma_j u_j$ , where  $u_j$  is the effective velocity given by (Draine 1986)

$$u_j = [\varphi_j + |\mathbf{v}_j - \mathbf{v}|^2]^{1/2}, \quad (17)$$

where

$$\varphi_j = \frac{128}{9\pi} \left( \frac{kT}{m_N} + \frac{kT_j}{m_j} \right). \quad (18)$$

The treatment of  $\langle \sigma v \rangle_j$  for each charges species is discussed further below in Section 5.

Equation (15) can be recast in terms of the electric field  $\mathbf{E}'$  in the frame co-moving with the neutrals,

$$\frac{\mathbf{v}_j - \mathbf{v}}{c} = \beta_j \frac{(\mathbf{B} \cdot \mathbf{E}') \mathbf{B}}{B^3} + \frac{\beta_j^2}{1 + \beta_j^2} \frac{\mathbf{E}' \times \mathbf{B}}{B^2} + \frac{\beta_j}{1 + \beta_j^2} \frac{\mathbf{B} \times (\mathbf{E}' \times \mathbf{B})}{B^3}, \quad (19)$$

where

$$\mathbf{E}' = \mathbf{E} + \mathbf{v} \times \mathbf{B}/c \quad (20)$$

and  $\beta_j$ , the Hall parameter for species  $j$ ,

$$\beta_j = \frac{Z_j e B}{m_j c} \frac{1}{\gamma_j \rho} \quad (21)$$

is the product of the gyrofrequency and the time-scale for momentum exchange with the neutral fluid.

Integrating the mass conservation equations (1) and (12) along with charge neutrality (14) gives (the subscript  $k$  runs over the ions and grains):

$$\rho v_z = \rho_0 v_s \quad (22)$$

$$\rho_k v_{zk} = \rho_0 v_s \quad (23)$$

$$n_e = n_i + \sum_g Z_g n_g, \quad (24)$$

where a local equilibrium approximation is used for  $Z_g$  (equation 56). Combining equations (2) with equations (6)-(8), and integrating, gives the neutral velocity components:

$$v_x = \frac{1}{\rho_0 v_s} \left[ \frac{B_z}{4\pi} (B_x - B_{0x}) \right], \quad (25)$$

$$v_y = \frac{1}{\rho_0 v_s} \left[ \frac{B_y B_z}{4\pi} \right], \quad (26)$$

and

$$v_z = \frac{1}{\rho_0 v_s} \left[ P_0 - P + \rho_0 v_s^2 + \frac{1}{8\pi} (B_{0x}^2 - B_x^2 - B_y^2) \right]. \quad (27)$$

Equations (2) and (3) are combined, along with (11), to construct an ODE in  $P$ :

$$\begin{aligned} \frac{dP}{dz} v_z \left( 1 - \frac{c_s^2}{v_z^2} \right) &= (\gamma - 1)(G - \Lambda) \\ &+ \frac{\gamma P}{4\pi \rho_0 v_s} \left[ B_x \frac{dB_x}{dz} + B_y \frac{dB_y}{dz} \right], \end{aligned} \quad (28)$$

where  $c_s$  is the neutral sound speed

$$c_s = \left( \frac{\gamma P}{\rho} \right)^{1/2}. \quad (29)$$

Equation (28) breaks down at the sonic point  $v_z = c_s$ .

Finally, from equations (4) and (5),

$$E_x = 0, \quad E_y = -\frac{v_s}{c} B_{0x} \quad (30)$$

and

$$B_z = B_{0z} = \cos \theta. \quad (31)$$

Integrating equation (20), and using (30);

$$E'_x = (v_y B_z - v_z B_y) \frac{1}{c} \quad (32)$$

and

$$E'_y = (-v_s B_{0x} + v_z B_x - v_x B_z) \frac{1}{c}. \quad (33)$$

Charge neutrality (equation 14) is used to find  $E'_z$  (see Section 7).

The shock problem then comprises of three ODE's in  $B_x$ ,  $B_y$ , and  $P$  equations (6), (7), and (28), respectively, with the algebraic relations (22), (25)-(27) for the neutral density and neutral velocity components, respectively, along with equations (31)-(33) for  $B_z$ ,  $E'_x$  and  $E'_y$ . To calculate the

right hand side of the ODE's (6) and (7), the current density components  $J_x$  and  $J_y$  need to be known, which are dependent upon the drift velocities,  $\mathbf{v}_j - \mathbf{v}$  (equation (13)). Calculating  $\mathbf{v}_j - \mathbf{v}$  from equation (19) requires knowledge of the Hall parameters  $\beta_j$ , as well as the electric field component  $E'_z$ . The treatment of  $\beta_j$  and  $E'_z$  are described below in Sections 5, 6, and 7. The heating and cooling rates needed for the energy equation (28) are discussed in Section 4.

### 3 JUMP CONDITIONS

The boundary conditions for equations (6), (7), and (28) are that the derivatives vanish far upstream and downstream of the shock. Shock solutions begin and end at points where

$$\frac{dB_x}{dz} = \frac{dB_y}{dz} = \frac{dP}{dz} = 0. \quad (34)$$

From equations (6)-(8),  $\mathbf{J} = 0$ , and equations (13) and (19) give  $\mathbf{E}' = 0$  and  $\mathbf{v}_j - \mathbf{v} = 0$ . All species are co-moving upstream and downstream of the shock and obey the same overall jump conditions. Also Equation (28) gives  $G = \Lambda$ .  $\mathbf{E}' = 0$ , so  $\mathbf{E} = -\mathbf{v} \times \mathbf{B}/c$  and by equations (32) and (33);

$$v_y B_z - v_z B_y = 0 \quad (35)$$

and

$$v_z B_x - v_x B_z = v_s B_{0x}. \quad (36)$$

Eliminating  $v_y$  from equations (26) and (36) gives either

$$B_y = 0 \quad \text{or} \quad (37)$$

$$v_z = \frac{B_z^2}{4\pi \rho_0 v_s}. \quad (38)$$

The second solution implies  $v_z$  is equal to the intermediate speed, resulting in a rotational discontinuity and no compression across the shock (Cowling 1976). So taking  $B_y = 0$  gives the condition  $v_y = 0$  ahead of and behind the shock.

In a radiative shock, the downstream fluid radiates away the energy transferred to it by the processes inside the shock. Cooling proceeds at a rate  $\Lambda(\rho, T)$  (Section 4) over a post shock cooling layer. Drift of the charged particles inside the shock lead to increases in thermal energy due to elastic scattering between the charged and neutral components. The immediate post-shock temperature is therefore much higher than the final post-shock temperature after the fluid has radiated away the energy inside the post-shock cooling layer.

The fluid cools inside the cooling layer at an almost constant pressure as the density increases and fluid speed decreases. The post-shock fluid cools until it returns to the pre-shock temperature  $T_0$ . Applying the isothermal jump conditions  $T = T_0$  along with equations (9) and (22) gives

$$\frac{P}{P_0} = \frac{n}{n_0} = \frac{v_s}{v_z}. \quad (39)$$

Equations (25), (27), (36), and (39) give a cubic in  $v_z/v_s$

$$\frac{v_z^3}{v_s^3} + a_0 \frac{v_z^2}{v_s^2} + a_1 \frac{v_z}{v_s} + a_2 = 0, \quad (40)$$

where

$$a_0 = -\frac{1}{2M_{A0}^2} (3\mu^2 + 1) - \frac{1}{\gamma M_{s0}^2}, \quad (41)$$

$$a_1 = \frac{1}{M_{A0}^2} \left[ \frac{2\mu^2}{\gamma M_{s0}^2} + \frac{\mu^2}{M_{A0}^2} - \frac{(1 - \mu^2)}{2} \right], \quad (42)$$

and

$$a_2 = -\frac{1}{\gamma} \frac{\mu^4}{M_{s0}^2 M_{A0}^4}. \quad (43)$$

Only roots with  $0 < v_z/v_s < 1$  are suitable for there to be compression across the shock. Once the downstream  $v_{zd}$  is calculated, the corresponding  $P$ ,  $B_x$ , and  $v_x$  are easily found. One could alternatively obtain a cubic in  $B_x$  and firstly solve for the downstream component  $B_{xd}$  instead.

#### 4 HEATING AND COOLING PROCESSES

The main heating processes inside dense molecular clouds are the heating by cosmic rays and heating from shocks. The cosmic ray heating rate is (Goldsmith & Langer 1978)

$$G_{cr} = 6.4 \times 10^{-28} n(\text{H}_2) \text{ ergs cm}^{-3} \text{ s}^{-1}. \quad (44)$$

Elastic scattering between two species at different temperatures will lead to heat exchange, as well as heat generation if the species are streaming relative to each other. The heating rate per unit volume produced by elastic scattering of a species  $\alpha$  with a species  $\beta$ , is (Draine 1986)

$$G^{\alpha\beta} = \frac{\rho_\alpha \rho_\beta}{(m_\alpha + m_\beta)} \gamma_{\alpha\beta} [3k(T_\beta - T_\alpha) + m_\beta |\mathbf{v}_\alpha - \mathbf{v}_\beta|^2], \quad (45)$$

where

$$\gamma_{\alpha\beta} = \frac{\langle \sigma v \rangle_{\alpha\beta}}{(m_\alpha + m_\beta)}. \quad (46)$$

If a species  $j$  is unable to cool efficiently and has a small heat capacity per unit volume then  $G^{jn} = 0$  (Chernoff 1987) and

$$T_j = T + \frac{1}{3k} m_n |\mathbf{v}_j - \mathbf{v}|^2. \quad (47)$$

The heating rate of the neutrals due to species  $j$  is then

$$G^{nj} = \rho \rho_j \gamma_j |\mathbf{v} - \mathbf{v}_j|^2. \quad (48)$$

Thus, by equation (15), the total heating rate is

$$G^n = \rho \sum_j \rho_j \gamma_j |\mathbf{v} - \mathbf{v}_j|^2 = \mathbf{J} \cdot \mathbf{E}', \quad (49)$$

The low mass of the electrons ensures that their collisional heating is negligible. With low fractional ionisation the grains dominate the collisional heating (Draine et al. 1983). The total neutral heating rate is then  $G = G^n + G_{cr}$ . The dominant cooling mechanisms inside shock-heated regions is collisional excitation of molecular H<sub>2</sub>. Neglecting the vibrational cooling, which is negligible for  $n(\text{H}_2) \lesssim 10^7 \text{ cm}^{-3}$   $T \lesssim 3000 \text{ K}$ , we adopt the cooling rate

$$\Lambda = n(\text{H}_2) \frac{L_{rH} L_{rL}}{L_{rH} + L_{rL}} \text{ ergs cm}^{-3} \text{ s}^{-1}, \quad (50)$$

with the rotational cooling rate coefficients for high and low density,  $L_{rH}$  and  $L_{rL}$ , from equations (10) and (11) of Lepp & Shull (1983).

#### 5 CHARGED SPECIES

##### 5.1 Ions and Electrons

The ions are singly charged with  $m_i = 30m_H$ . As discussed in Wardle (1998), the scattering cross-section  $\sigma_i$

has a  $1/v$  dependence for drift speeds below 20km/s, and the rate coefficient for ion-neutral scattering is  $\langle \sigma v \rangle_i \approx 1.6 \times 10^{-9} \text{ cm}^3 \text{ s}^{-1}$ . The ion Hall parameter (equation (21)) can thus be written in terms of the pre-shock Hall parameter

$$\beta_i = \beta_{i0} \frac{B}{B_0} \frac{v_z}{v_s}. \quad (51)$$

Inside a molecular cloud (Elmegreen 1979)

$$\frac{n_i}{n_H} \approx 10^{-8} \left( \frac{n_H}{10^6 \text{ cm}^{-3}} \right)^{-1/2}. \quad (52)$$

The ions are unable to cool efficiently, as they have a small heat capacity per unit volume, due to the low fractional ionisation, thus  $G^{ni} \approx 0$  and equation (47) applies to  $T_i$ . The electron scattering cross-section is  $\sigma_e \approx 1 \times 10^{-15} \text{ cm}^2$ , and as  $m_e \ll m_n$ , then by equation (17):

$$u_e = [\varphi_e + |\mathbf{v}_e - \mathbf{v}|^2]^{1/2}, \quad (53)$$

where

$$\varphi_e = \frac{128}{9\pi} \frac{kT_e}{m_e}. \quad (54)$$

The electron temperature  $T_e$  is needed to calculate  $u_e$  and  $Z_g$ . Electrons and ions are highly coupled to  $\mathbf{B}$  with  $|\beta_{i,e}| \gg 1$  (equation (21)), and thus  $(\mathbf{v}_i - \mathbf{v}) \approx (\mathbf{v}_e - \mathbf{v}) \approx \mathbf{E}' \times \mathbf{B}/B^2$  (equation (19)). Equation (47), therefore, implies that  $T_e \approx T_i$ , however Draine et al. (1983) showed that inside shocks in dense molecular gas the electrons lose energy due to impact excitation of H<sub>2</sub> and  $T_e < T_i$ .  $T_e$  is therefore approximated via (see Fig. 1 of Draine et al. (1983))

$$T_e \approx T + 0.2(T_i - T). \quad (55)$$

Once  $T_e$ , and subsequently  $u_e$ , are known, then  $\beta_e$  can be determined. The calculation of  $\beta_e$  is complicated by the dependence of  $u_e$  on  $|\mathbf{v}_e - \mathbf{v}|$ . To determine  $\beta_e$ , equations (17), (19), and (21) must be solved, this is discussed in Section 6.

##### 5.2 Grains

The charge on a dust grain  $Z_g$  results from collisions with other charged particles as well as the ejection of photoelectrons. The charge state of a grain contains stochastic fluctuations about some mean (Spitzer 1978; Gail & Sedlmayr 1975). If the fluctuations are neglected, the instantaneous mean charge on a dust grain of radius  $a_g$  is (Draine 1980)

$$Z_g \approx \frac{-4kT_e a_g}{e^2}. \quad (56)$$

Equation (56) is only valid for  $|Z_g| \gg 1$  which is not always satisfied for the pre-shock conditions of interest; in cold molecular clouds  $T_{e0} = 10 \text{ K}$  and for a MRN distribution  $a_g = [50 \text{ \AA}, 2500 \text{ \AA}]$ ,  $|Z_{g0}| < 1$ . We force  $Z_g = -1$  when  $|Z_g| < 1$  by equation (56). The scattering cross-section for a spherical grain is  $\sigma_g = \pi a_g^2$ , and by equation (17),

$$u_g = \left[ \frac{128}{9\pi} \left( \frac{kT}{m_N} \right) + |\mathbf{v}_g - \mathbf{v}|^2 \right]^{1/2}, \quad (57)$$

as the grain thermal velocity is negligible compared with that of the neutrals. The internal density is  $2.5 \text{ g/cm}^3$ . By equation (56) the relative gyrofrequency ( $Z_g e B / m_g c$ ) for a smaller grain  $a_{gs}$  is greater than that of a larger grain  $a_g$ ,

by  $(a_{gl}/a_{gs})^2$ , and so the smaller grains remain better coupled to the field. Consequently, the smallest grains have the largest  $\beta_g$ . The calculation of  $\beta_g$  is addressed in Section 6.

The abundance of the pre-shock grains is given by a MRN grain size distribution (Mathis, Rumpl & Nordsieck 1977) which assumes a mixture of silicate and graphite;

$$\frac{dn_{g0}}{da} = An_H a^{-3.5}, \quad A = 1.5 \times 10^{-25} \text{ cm}^{2.5}. \quad (58)$$

The limits are  $[a_1, a_2] = [50\text{\AA}, 2500\text{\AA}]$  and defining  $y = \log a$ ;

$$x_{G0} = \frac{n_{g0}}{n_H} = \int_{a_1}^{a_2} A a^{-3.5} da = \int_{\log a_1}^{\log a_2} A a^{-2.5} dy. \quad (59)$$

Inside dense molecular clouds, the grain size distribution may differ considerably from the MRN model (e.g. Li & Greenberg 2003). Observational measurements of the visible extinction of objects behind dense clouds suggest that larger dust grains may be present (e.g. Whittet et al. 1983). Inside dense clouds, the growth of ice mantles and dust coagulation can remove the smaller grains ( $a_g << 1000\text{\AA}$ ), and can increase the grain mass by a factor of up to 2 (Chokshi et al. 1993). We also consider a MRN distribution with increased limits  $[a_{1m}, a_{2m}] = [90\text{\AA}, 4500\text{\AA}]$  (Nishi, Nakano & Umebayashi 1991). The distribution is re-normalised with  $A_{mantles} a_m^{-2.5} = A a^{-2.5}$  so  $A_{mantles} = A(a/a_m)^{-2.5} = 6.5 \times 10^{-25} \text{ cm}^{2.5}$  and the mean interior density is  $1.14 \text{ g/cm}^3$ .

Using Gauss-Legendre weights (a highly accurate method of integrating smooth functions) the MRN grain size distribution may be represented by the summation over a number of discrete grain bins or grain size classes (Press et al. 1992) and equation (59) may be expressed as

$$x_{G0} = \int_{\log a_2}^{\log a_1} f(y) dy = \sum_{m=1}^N w_m f(y_m) = \sum_{m=1}^N x_{g0m}, \quad (60)$$

where  $y_m$  are abscissae with weights  $w_m$ ,  $f(y) = A a^{-2.5}$ , and  $y = \log a$ . The  $y_m$  and  $w_m$  are pre-determined from the Legendre polynomial of order N. Each of the N grain bins, have an associated size  $a$ , number density  $x_{g0m}$ , and corresponding parameters,  $Z_{gm}$ ,  $\beta_{gm}$ ,  $v_{gxm}$ ,  $v_{gym}$ , and  $v_{gzm}$ . Using equation (60), any integrals over the grain size distribution can be generalised such that for any function  $g(y)$ ;

$$\int_{\log a_2}^{\log a_1} f(y) g(y) dy = \sum_{m=1}^N w_m f(y_m) g(y_m) = \sum_{m=1}^N x_{g0m} g(y_m). \quad (61)$$

Equations (49) and (13) are calculated in this way, for example;

$$\mathbf{J} = en_H \left[ x_i \mathbf{v}_i - x_e \mathbf{v}_e + \sum_{m=1}^N x_{g0m} \frac{v_s}{v_{zgm}} Z_{gm} \mathbf{v}_{gm} \right]. \quad (62)$$

## 6 HALL PARAMETERS

To determine  $\beta_e$  and  $\beta_g$ , equations (17), (19), and (21) are solved as follows. Writing

$$\mathbf{E}'_{||} = \frac{(\mathbf{B} \cdot \mathbf{E}')}{B^3} \mathbf{B} \quad (63)$$

and

$$\mathbf{E}'_{\perp} = \frac{\mathbf{B} \times (\mathbf{E}' \times \mathbf{B})}{B^3} = \frac{\mathbf{E}'}{B} - \frac{(\mathbf{B} \cdot \mathbf{E}')}{B^3} \mathbf{B}, \quad (64)$$

then the drift velocity equation (19) may be written as

$$\frac{\mathbf{v}_j - \mathbf{v}}{c} = \beta_j \mathbf{E}'_{||} + \frac{\beta_j^2}{1 + \beta_j^2} \frac{\mathbf{E}'_{\perp} \times \mathbf{B}}{B^2} + \frac{\beta_j}{1 + \beta_j^2} \mathbf{E}'_{\perp}. \quad (65)$$

Taking the dot product of  $\mathbf{v}_j - \mathbf{v}$  with itself gives

$$|\mathbf{v}_j - \mathbf{v}|^2 = \beta_j^2 \mathbf{E}'_{||}^2 c^2 + \frac{\beta_j^2}{1 + \beta_j^2} \mathbf{E}'_{\perp}^2 c^2. \quad (66)$$

Defining  $\alpha_j$  as

$$\alpha_j = \frac{Z_j e B}{m_j c} \frac{m_j + m}{\sigma_j \rho}, \quad (67)$$

then equation (21) becomes

$$\beta_j = \frac{Z_j e B}{m_j c} \frac{(m_j + m)}{\sigma_j u_j \rho} = \frac{\alpha_j}{u_j}, \quad (68)$$

Eliminating  $u_j$  from equation (68) using (17) gives

$$|\mathbf{v}_j - \mathbf{v}|^2 = \frac{\alpha_j^2}{\beta_j^2} - \varphi_j. \quad (69)$$

After eliminating  $|\mathbf{v}_j - \mathbf{v}|$  from equations (66) and (69) then

$$\begin{aligned} \beta_j^6 \mathbf{E}'_{||}^2 + \beta_j^4 \left( \mathbf{E}'_{||}^2 + \mathbf{E}'_{\perp}^2 + \frac{\varphi_j}{c^2} \right) \\ + \beta_j^2 \left( \frac{\varphi_j}{c^2} - \frac{\alpha_j^2}{c^2} \right) - \frac{\alpha_j^2}{c^2} = 0, \end{aligned} \quad (70)$$

which has only one positive root for  $\beta_j^2$ . The root  $-|\beta_j|$ , is then taken for the negatively charged electrons and grains.

## 7 CALCULATING $E'_z$

Lastly,  $E'_z$  is needed, and using equations (14) and (23), equation (19) is recast in terms of  $v_{jz}$  (Wardle 1998):

$$v_{jz} = n_{j0} Z_j (p_j E'_z + q_j), \quad (71)$$

where

$$p_j = \frac{c}{n_{j0} Z_j} \frac{\beta_j}{1 + \beta_j^2} \frac{(B_z \beta_j^2 + B^2)}{B^3} \quad (72)$$

and

$$\begin{aligned} q_j = & \frac{1}{n_{j0} Z_j} \left[ v_z + \frac{c \beta_j^2}{1 + \beta_j^2} \frac{(\mathbf{E}' \times \mathbf{B})_z}{B^2} \right] \\ & + \frac{1}{n_{j0} Z_j} \frac{c \beta_j^3}{1 + \beta_j^2} (B_x E'_x + B_y E'_y) \frac{B_z}{B^3}. \end{aligned} \quad (73)$$

From equations (14), (23), and (71),

$$n_e = \sum_k Z_k n_{0k} \frac{v_s}{v_{jz}} = \sum_k \frac{v_s}{p_k E'_z + q_k} \quad (74)$$

where  $k$  runs over the grain and ion species. Also by equations (8) and (13);

$$0 = -n_e v_{ez} + \sum_k Z_k n_k v_{zk} = -n_e v_{ez} + v_s \sum_k Z_k n_{0k}. \quad (75)$$

Using equation (71) for the electrons with equation (75), and using equation (74) to eliminate  $n_e$  gives

$$\frac{1}{(p_e E'_z + q_e)} \sum_k \frac{n_{0k} Z_k}{n_{e0}} + \sum_k \frac{1}{p_k E'_z + q_k} = 0. \quad (76)$$

Equation (76) has  $N$  poles at  $E'_z = -q_j/p_j$ , with  $N-1$  solutions for  $E'_z$ . In Wardle (1998),  $N=3$  and equation (76) is an easily solvable quadratic in  $E'_z$ . For arbitrary  $N$  the choice of the correct root for  $E'_z$  is not so simple. Imposing the requirement  $E'_z = 0$  upstream and downstream enables the identification of the bracketing pole species ( $-q_{j0}/p_{j0}$ ). Since  $E'_z$  is continuous through the shock, the correct  $E'_z$  root will remain between these bracketing species poles. Since

$$p_{j0} = \frac{c}{n_{j0}Z_{j0}} \frac{\beta_{j0}}{1 + \beta_{j0}^2} \frac{1}{B_0} \left[ \frac{B_z^2 \beta_{j0}^2}{B_0^2} + 1 \right], \quad (77)$$

$$q_{j0} = \frac{1}{n_{j0}Z_{j0}} v_s, \quad (78)$$

then  $p_{j0} < 0$  and the sign of  $q_{j0}$  is determined by the sign of  $Z_{j0}$ . The ion pole  $-q_{i0}/p_{i0}$  will always be negative, however poles of the negatively charged species are positive, thus  $-q_{i0}/p_{i0}$  will always be the minimum bracketing pole.  $\beta_{e0} \sim 10^3$  and  $\beta_{g0} \sim 10^1 - 10^2$  for the grain sizes considered, so  $|q_{e0}/p_{e0}| < |q_{g0}/p_{g0}|$ . Thus the solution for  $E'_z$  is the root of equation (76) that lies between  $-q_i/p_i$  and  $-q_e/p_e$ .

## 8 SHOCK CALCULATIONS

All fluid variables are made dimensionless by expressing the velocity, magnetic field, electric field, and pressure in units of  $v_s$ ,  $B_0$ ,  $v_s B_0/c$ , and  $P_0/(\rho v_s^2)$ , respectively. The characteristic length scale of the shock is (Wardle 1998)

$$L_s = \frac{v_{A0}}{\sum_j \gamma_{j0} \rho_{j0}}. \quad (79)$$

The shock models are calculated as follows. For the MRN grain size distribution models,  $x_{g0}$  is assigned to each grain class (Section 5.2).  $x_{e0}$  is then calculated from charge neutrality (equation (14)), and  $\beta_{e0}$ ,  $\beta_{i0}$  and  $\beta_{gm0}$  are calculated (equation (21)). The appropriate root of the isothermal jump condition (equation (40)) for downstream  $v_{zd}$  is found, allowing the calculation of downstream  $v_x$ ,  $P$ , and  $B_x$  from equations (25), (27) and (39). The pole bracketing species for  $E'_z$  is identified as described in Section 7.

As discussed in Wardle (1998), a one parameter family of solutions exist and integration from upstream to downstream yields the intermediate shock solutions, and from downstream to upstream gives the desired fast shock solution. Integration of the ODE's for  $B_x$ ,  $B_y$ , and  $P$ , equations (6), (7), and (28), respectively, are then performed after perturbing these quantities from the downstream state. The equations are stiff so the integration method of Gear (1971) is used. For each step, the integrator produces values for  $B_x$ ,  $B_y$  and  $P$ , enabling the calculation of  $v_x$ ,  $v_y$ ,  $v_z$ ,  $E'_x$  and  $E'_y$  directly from equations (25)-(27) and (32)-(33). Finding solutions to equation (70) for  $\beta_e$  and  $\beta_{gk}$  and equation (76) for  $E'_z$ , are complicated by their mutual dependence. To find a solution, the value of  $E'_z$  obtained in the last step of the integrator is used as a starting value. The corresponding Hall parameter (equation (69)) is found (using the updated values of  $B_x$ ,  $B_y$ ,  $E'_x$ , and  $E'_y$ ), including the corresponding bracketing poles for equation (76). The accuracy of this value for  $E'_z$  as a root of equation (76) can then be tested. If tolerances are not met, the value of  $E'_z$  is amended and the process repeated until required numerical

accuracy is reached. Once  $E'_z$  and  $\beta_{i,e,g}$  are known,  $\mathbf{v}_{i,e,g} - \mathbf{v}$  are calculated (equation (19)), enabling the calculation of the current density (equation (13)). The heating and cooling rates, (equations (45) and (50)), can also be found. The right hand sides of equations (28), (6), and (7), can then be evaluated and passed to the integrator.

The calculation of radiative shocks is complicated by the long length scales required over which the shock cools to its post-shock temperature. The jump conditions yield the downstream state of the shock but integration cannot proceed directly from this state as the length scales for the shock to cool after the other dynamic variables relax is too large. Relaxation methods have been implemented in the past for this reason (Draine 1980), requiring the determination of the fluid variables on grid points in  $B_x - B_y - P$  space and then the variables are ‘relaxed’ until the correct solution is reached that satisfies the boundary jump conditions. This method is inapplicable here since the calculation of  $E'_z$  requires an initial guess at each point on the shock and an arbitrary choice of  $E'_z$  will not always satisfy bracketing pole criteria of equation (76). Integration through the shock however, provides the initial guess for  $E'_z$ , which is sufficiently close to the desired solution and satisfies the pole criteria.

The alternative we have implemented is to search for the solution from upstream of the final post-shock state, before radiative cooling is dominant. An initial starting state for  $(B_x^*, B_y^*, P_d^*)$  is chosen in which  $B_x$  and  $B_y$  should have almost obtained their post-shock values;  $B_y \approx 0$  and  $B_x^* = B_{xd} + \delta B_x$ , where  $\delta B_x$  is small ( $\sim 1\%$  of  $B_{xd}$ ). The pressure  $P^* = P_d + \delta P_d$  is given a larger relative perturbation and the radiative cooling zone is stepped over. It is unlikely that integration from this approximate state will yield the correct solution, but it acts as a good initial guess. The calculation is a two point boundary problem with a known desired final (upstream) state and the (downstream) initial values need to be adjusted until integration from downstream to upstream yields the correct fast shock solution. This is done by using the shooting method (Press et al. 1992) which repeatedly performs the integration for adjusted initial states. The initial starting parameters  $(B_x^*, B_y^*, P_d^*)$  are free variables, and the upstream variables  $(B_{x0}, B_{y0}, P_0)$  are fixed. The shooting method proceeds by using a multi-dimensional Newton-Raphson root finder which zeros three functions obtained by integrating the ODEs in  $B_x$ ,  $B_y$ , and  $P$  over the domain of integration.

A requirement of the shooting method is that for each initial guess  $(B_x^*, B_y^*, P_d^*)$ , the subsequent shot can transverse the entire domain of integration. This is not always the case for very wrong initial guesses, and physically impossible states may be reached (e.g.,  $T$  or  $x_e$  may go negative). The convergence of the solution is complicated by unsuccessful integration shots. Fortunately, for any number integration shots there was clear convergence, before the trajectories diverged. A multiple shooting method was therefore implemented which after convergence did occur, restarts the shooting process at a point inside the shock using values derived from the converged solution from the previous shooting procedure. This process is repeated through the domain of integration, until the upstream state is reached.

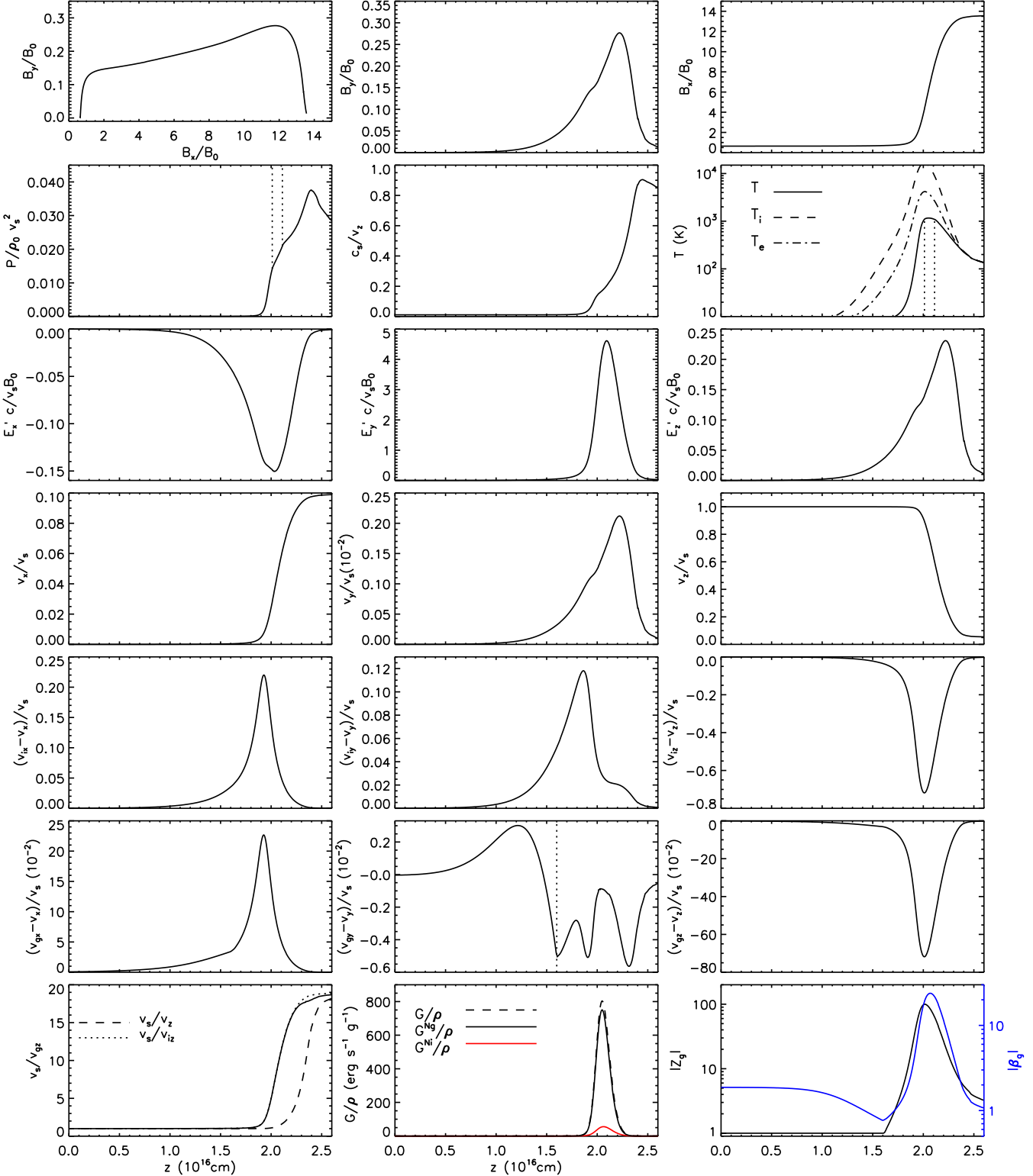


**Figure 1.** Single sized grain shock model with grain radius  $0.1\mu\text{m}$ ,  $n_g/n_H = 1.6 \times 10^{-12}$ , and  $\theta = 40^\circ$ . Shown are the magnetic field components  $B_x$ ,  $B_y$ , the neutral pressure  $P$ , ratio  $c_s/v_z$  and temperatures  $T$ ,  $T_i$  and  $T_e$ . Also plotted are the electric field components in the neutral frame  $E'_x$ ,  $E'_y$ , and  $E'_z$ , the neutral velocity components  $v_{x,y,z}$ , and the charged species drift velocity components  $(v_{ix,y,z} - v_{x,y,z})$  and  $(v_{gx,y,z} - v_{x,y,z})$ . The grain parameters  $Z_g$  and  $\beta_g$ , are shown along with the compression ratios  $v_s/v_{jz}$  and the heating rates per unit mass,  $G^{nj}/\rho$ .

## 9 RESULTS: C-TYPE SHOCK MODELS

C-type shock profiles are presented assuming both small and large single sized grains (Sections 9.1 and 9.3) as well as the MRN grain size distribution with and without mantles and PAHs (Sections 9.4, 9.5 9.6).  $\theta$  is varied in Sections 9.2 and 9.4, and the effects of suppressing  $B_y$  are demonstrated in Section 9.7. Unless stated otherwise, the pre-shock conditions are:  $B_0 = 0.3\text{mG}$ ,  $n_H = 10^5\text{cm}^{-3}$ ,  $n_0 = n(\text{H}_2) + n(\text{H}) + n(\text{He}) \approx 0.5n_H + 0.1n_H = 0.6n_H$ ,  $n_{i0}/n_H = 3 \times 10^{-8}$  (by equation (52)),  $\gamma = 7/5$  (see the discussion near equation (11)), and  $T_0 = T_{e0} = T_{i0} = 10\text{K}$ . The shock speed is  $v_s = 18\text{km/s}$

### 9.1 Single sized small $a_g = 0.1\mu\text{m}$ grain model

A single grain species,  $a_g = 0.1\mu\text{m}$  and internal density of  $2.5\text{g/cm}^3$ , is now considered. If the total mass of the grains is 0.01 that of hydrogen (Draine et al. 1983),  $n_{g0}/n_H = 1.6 \times 10^{-12}$  (Wardle 1998).  $n_{i0}/n_H = 3 \times 10^{-8}$  and  $n_{e0}/n_H = 2.99984 \times 10^{-8}$  by charge neutrality (equation (14)). Then  $\beta_{i0} = 1.382 \times 10^4$ ,  $\beta_{e0} = -3.358 \times 10^7$ , and  $\beta_{g0} = -1.632$ . Fig. 1 shows a shock profile with  $\theta = 40^\circ$ . The  $B_x - B_y$  phase plot shows the shock transition from the upstream state  $(B_{x0}, B_{y0}) = (0.7, 0)B_0$  to the downstream state  $(B_{xd}, B_{yd}) = (13.7, 0)B_0$ . The rotation of  $\mathbf{B}_\perp$  out of and back into the  $x - z$  plane is easily identified.

Initially  $B_y$  then  $B_x$  increase (from upstream to downstream) near  $z = 1 \times 10^{16}\text{cm}$ , resulting in an increase of  $B_\perp$ . As  $B_\perp^2/(2B_0^2M_{A0}^2) + v_z/v_s + P/(\rho_0v_s^2)$  is constant (by equation (27)), and changes in  $P/(\rho_0v_s^2)$  are relatively small in this part of the shock there is a compensatory decrease in  $v_z/v_s$ . The compression of the neutral fluid begins, and  $P$  and  $T$  begin to increase.  $T_e$  and  $T_i$  also increase, and the approximation used for  $T_e$  (equation (55)) leads to a maximum of  $\sim 4000\text{ K}$ , consistent with Draine et al. (1983).

The ODE for  $P$  is sensitive to the compression of the neutral fluid, and the balance of  $G - \Lambda$  with the magnetic gradient terms of equation (28). The  $G - \Lambda$  term dominates in equation (28). Initially  $P$  increases as the neutral fluid is compressed and heated.  $T$  decreases after  $z = 2.05 \times 10^{16}\text{cm}$ , but  $P$  continues to rise since there is still compression.  $P$  does not fall until  $z = 2.4 \times 10^{16}\text{cm}$  when the compression slows, and  $v_z/v_s$  reaches its downstream value.  $T$  and  $P$  have not yet reached their post-shock states in Fig. 1, and will not reach them until far downstream of the shock, after the neutral fluid cools inside the radiative zone.

The  $P$  profile shows two discontinuities in  $dP/dz$  at  $z = 2 \times 10^{16}\text{cm}$  and  $z = 2.1 \times 10^{16}\text{cm}$ , indicated by dotted lines. These occur at  $T = 1087\text{K}$  and are artefacts of the cooling function (equation (50)) which is discontinuous at  $T = 1087\text{K}$  (Lepp & Shull 1983). Interpolation of  $\Lambda$  was used to smooth the transition at  $T = 1087\text{K}$ , however  $P$  is highly sensitive to  $\Lambda$ , still reflecting the discontinuity in  $\Lambda$ .

Fig. 1 shows the ratio  $c_s/v_z$  nearing the sonic condition at  $z = 2.45 \times 10^{16}\text{cm}$  ( $c_s/v_z \sim 0.9$ ). The peak coincides with the slowing of the compression as  $v_z$  approaches the downstream value.  $c_s/v_z$  then decreases as  $c_s$  decreases with  $T$ .  $v_z = c_s$  if the neutral fluid cools quickly enough after the peak in  $T$ . This occurs for certain pre-shock conditions, e.g., high pre-shock number densities and/or low  $\theta$ . In this case, the shock becomes either C\*-type or J-type, requiring dif-

ferent numerical procedures to calculate the shock structure since equation (28) cannot be integrated through the critical point (Roberge & Draine (1990)).

In Fig.1,  $E'_x$  and  $E'_z$  are similar in magnitude, with  $E'_y$  an order of magnitude larger. Since  $v_x \propto (B_x - B_{0x})$  and  $v_y \propto B_y$  (equation (26)), trends in  $v_x$  and  $v_y$  follow those of  $B_x$  and  $B_y$ .  $v_x$  steadily increases through the shock, before reaching the downstream state given by the jump conditions. The magnitude of  $v_y$  is orders of magnitude smaller than  $v_x$  and  $v_z$ . As  $\mathbf{E}'_\parallel = (\mathbf{B} \cdot \mathbf{E}')\mathbf{B}/B^3$  is negligible through the shock, and by equation (19)

$$\frac{\mathbf{v}_j - \mathbf{v}}{c} \approx \frac{\beta_j^2}{1 + \beta_j^2} \frac{(\mathbf{E}' \times \mathbf{B})}{B^2} + \frac{\beta_j}{1 + \beta_j^2} \frac{\mathbf{E}'}{B}. \quad (80)$$

For  $|\beta_j| \gg 1$  the species are tied to  $\mathbf{B}$  with  $(\mathbf{v}_j - \mathbf{v}) \approx (\mathbf{E}' \times \mathbf{B})c/B^2$ , as is the case for the ions and electrons. The ions (and electrons) lead the neutrals in the  $x$  and  $y$  directions but lag the neutrals in  $z$ . The second term in equation (80) becomes non-negligible for the grains with  $|\beta_g| \sim 1 - 10$ .  $(v_{iy} - v_y)$  has more structure than both  $(v_{ix,z} - v_{xz})$ . The shoulder at  $z \sim 2.2 \times 10^{16}\text{cm}$  where  $(v_{iy} - v_y)$  declines much less rapidly, corresponds to the peak of  $E'_z$  and a slowing down of the compression of  $B_x$  ( $B_x \approx B_{xd}$ ). As  $E'_z$  subsequently decreases after  $z = 2.25 \times 10^{16}\text{cm}$ , there is a corresponding reduction in  $(v_{iy} - v_y)$ .

$(v_{gx,z} - v_{xz})$  are shown in Fig. 1, and are similar in magnitude to  $(v_{ix,z} - v_{xz})$ .  $(v_{gy} - v_y)$  is an order of magnitude smaller than  $(v_{iy} - v_y)$  and contains oscillations. The ratios  $v_s/v_{jz}$  (equations (22) and (23)) show that the grains and ions are compressed ahead of the neutrals at  $z = 1.8 \times 10^{16}\text{cm}$  (along with  $\mathbf{B}$ ), with compression in the neutral fluid occurring after  $z = 2.0 \times 10^{16}\text{cm}$ .

The grain charge remains  $-1$  until  $T_e$  increases and  $|Z_g| > 1$  by equation (56). The peak in  $|Z_g|$  corresponds to the peak in  $T_e$ . Initially  $|\beta_g| \sim 1$ , but as the grain drift increases,  $u_g$  increases (equation (17)) and there is a decrease in  $|\beta_g|$ .  $|\beta_g|$  starts to increase when  $|Z_g|$  increases. As  $\mathbf{B}$  is compressed  $|\beta_g|$  increases further and the grains become better coupled to  $\mathbf{B}$ . The decrease in  $|\beta_g|$  after  $z = 2.1 \times 10^{16}\text{cm}$  follows the decrease in  $|Z_g|$  as  $T_e$  declines.

As  $|\beta_g| \sim 1 - 10$ ,  $\mathbf{v}_g - \mathbf{v}$  is dependent on the balance of terms in equation (80). When  $|\beta_g| \approx 1$  the second term reaches a maximum for a given  $\mathbf{B}$  and  $\mathbf{E}'$ , and  $\mathbf{v}_g - \mathbf{v}$  is determined by the balance of both terms. For  $|\beta_g| < 1$  both terms decrease with  $|\beta_g|$  and  $|\mathbf{v}_g - \mathbf{v}|$  decreases, signifying an increase in the grain-neutral coupling. The oscillations in  $(v_{gy} - v_y)$  are due to the balance of the competitive terms in equation (80). The sharp increase in  $(v_{gy} - v_y)$ , marked by the dotted line, corresponds to the increase in  $|Z_g|$  and  $|\beta_g|$ .  $G^{ng}$  dominates  $G$  in Fig. 1 with only a small contribution from  $G^{ni}$ .

### 9.2 $a_g = 0.1\mu\text{m}$ grain model: varying $\theta$

A comparison of the  $a_g = 0.1\mu\text{m}$  models for  $\theta = 40^\circ$ ,  $45^\circ$ ,  $60^\circ$ , and  $\theta = 80^\circ$ , is plotted in Fig. 2. The  $z$  offset in each  $\theta$  model is arbitrary, and the solutions have been shifted in  $z$  to overlay and compare. Since  $B_{x0} = B_0 \sin \theta$  the upstream state differs for each model. As  $\theta$  decreases from  $80^\circ$  to  $40^\circ$ , the amount of  $\mathbf{B}_\perp$  rotation increases as seen in the  $B_x - B_y$  phase plot.. For the  $\theta = 80^\circ$  model,  $B_y$

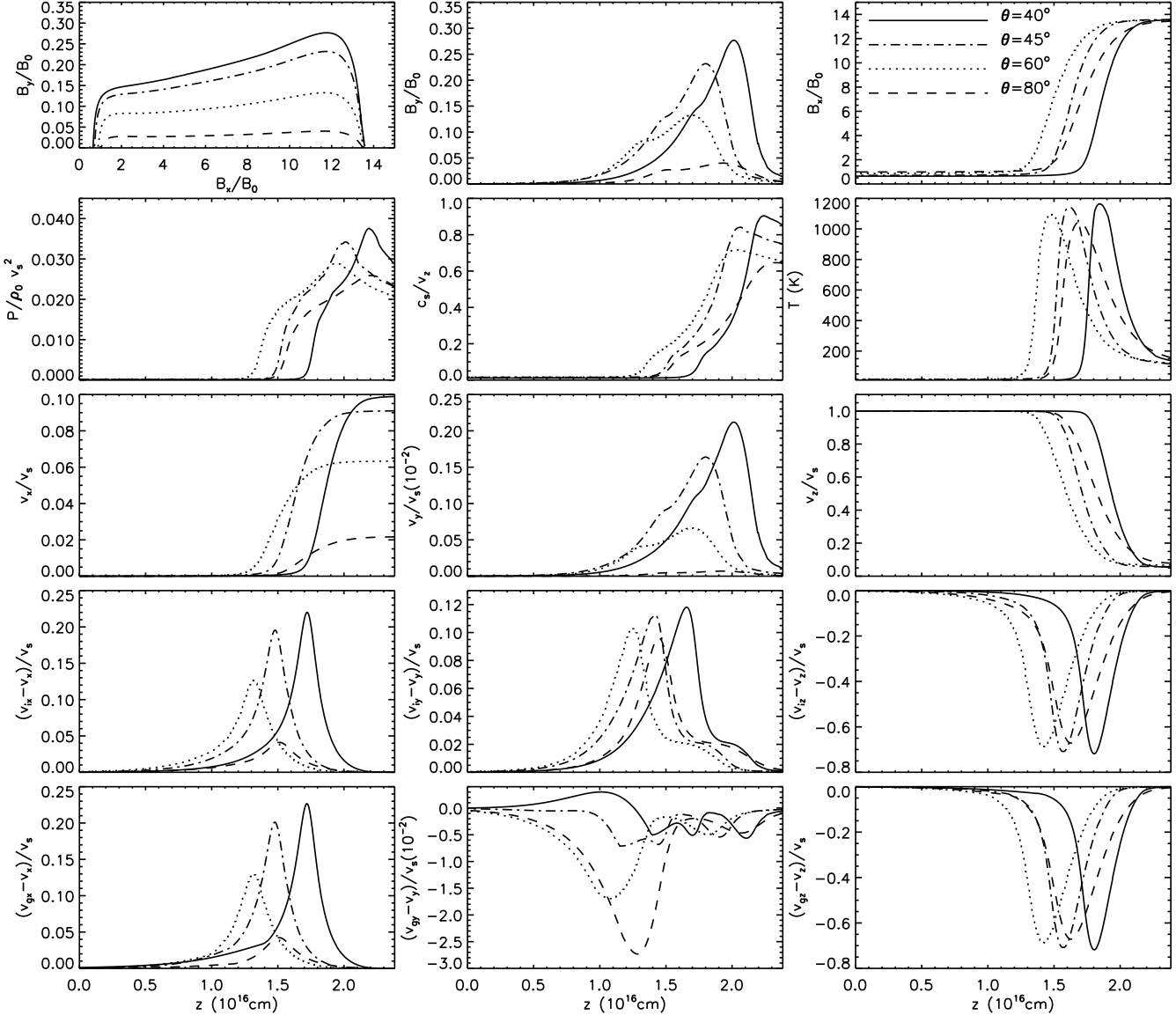


**Figure 2.** Comparison of  $\theta = 40^\circ$  (solid),  $45^\circ$  (dot-dash),  $60^\circ$  (dotted), and  $80^\circ$  (dashed) for the  $a_g = 0.1\mu\text{m}$  and  $n_g/n_H = 1.6 \times 10^{-12}$  model. The  $\theta = 40^\circ$  line series is the same as in Fig. 1. The descriptions of the quantities are the same as in the caption for Fig. 1.

and  $v_y$  are small, and the neutrals are restricted mainly to the  $x - z$  plane. Conversely, for  $\theta = 40^\circ$  there is maximum rotation of  $\mathbf{B}_\perp$  with largest  $B_y$  and  $v_y$ . The shock widths do not differ greatly with  $\theta$ . There are larger peaks in  $P$  and  $T$  as  $\theta$  is decreased. The neutrals approach a sonic point as  $\theta$  decreases, with the peak  $c_s/v_z \rightarrow 1$ . C-type solutions are restricted by the choice of  $\theta$ ,  $\theta_{critical} \sim 40^\circ$ , below which the neutral fluid becomes subsonic inside the shock.

The jump conditions are  $\theta$  dependent so the downstream values of  $v_x$  and  $v_z$  differ for each  $\theta$  model in Fig. 2. The differences in  $B_y$  and  $B_z$  with  $\theta$  leads to differences in  $(v_{ix} - v_x)$ , e.g., when  $\theta = 80^\circ$ , the peaks in  $B_z$  and  $B_y$ , and thus  $(\mathbf{E}' \times \mathbf{B})_x$  are small, leading to a lower peak  $(v_{ix} - v_x)$  (equation (80)).  $(v_{iy,z} - v_{y,z})$  show smaller differences, with the largest peak in  $|v_{iy,z} - v_{y,z}|$  for the low  $\theta = 40^\circ$  case.

$(v_{gx,z} - v_{x,z})$  are similar in magnitude to  $(v_{ix,z} - v_{x,z})$ , showing the same  $\theta$  dependent features. Differences in the structure of  $(v_{gy} - v_y)$  with  $\theta$  are large, and as  $\theta$  increases

from  $40^\circ$  to  $80^\circ$  the number of oscillations decreases and the relative peak magnitude increases.  $|Z_g|$  and  $|\beta_g|$  are comparable for all  $\theta$  (see Fig. 1), and differences in  $(v_{gx,y,z} - v_{x,y,z})$  are mainly due to the differences in  $\mathbf{E}'$  and  $\mathbf{B}$ .

### 9.3 Single sized large $a_g = 0.4\mu\text{m}$ grain model

Dust grains inside dense molecular clouds are larger than those in the diffuse interstellar medium (e.g., Carrasco et al. 1973) due to coagulation and the growth of ice mantles. The grain size is now increased to  $a_g = 0.4\mu\text{m}$  to represent grain growth via coagulation. Assuming the total mass of the grains is 0.01 that of hydrogen then  $x_{g0} = 2.5 \times 10^{-14}$  (Draine et al. 1983) and  $\beta_{g0} = -0.1020$ .  $x_{g0}$  and the net grain charge is decreased by two orders of magnitude compared with the  $a_g = 0.1\mu\text{m}$  model. The  $a_g = 0.1\mu\text{m}$  and  $a_g = 0.4\mu\text{m}$  models for  $\theta = 45^\circ$  are compared in Fig. 3. The  $0.4\mu\text{m}$  grains are less coupled to  $\mathbf{B}$ , so the rotation of  $\mathbf{B}_\perp$

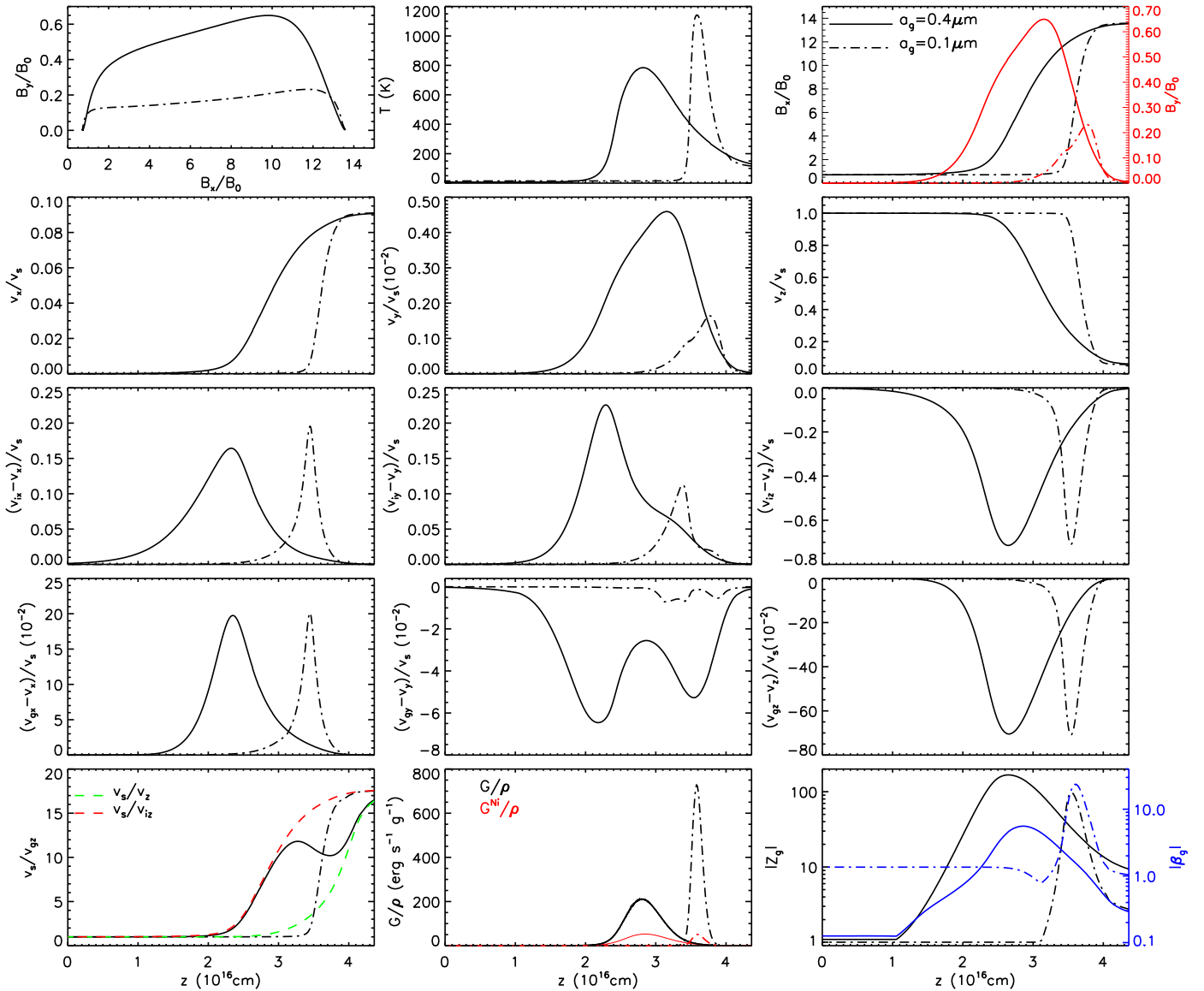


**Figure 3.** Comparison of  $\theta = 45^\circ$  single size grain models;  $a_g = 0.1\mu\text{m}$  with  $n_{g0}/n_H = 1.6 \times 10^{-12}$  (dot-dash) and  $a_g = 0.4\mu\text{m}$  with  $n_{g0}/n_H = 2.5 \times 10^{-14}$  (solid). The descriptions of the corresponding quantities are the same as in the caption of Fig. 1.

increases. The shock width is larger and there is a corresponding reduction in the peak temperature to  $T \sim 800\text{K}$ , as the same amount of kinetic energy flux must be dissipated into thermal energy as for the thinner  $0.1\mu\text{m}$  model shock.

The remaining variables plotted in Fig. 3 are consistent with the field components, e.g., there are larger peaks in  $|v_{iy,yz} - v_y|$  and  $v_y$ , consistent with larger  $B_y$ . There is also a steeper decrease (increases) in  $v_z$  ( $v_x$ ) for the smaller grain case than for the  $a_g = 0.4\mu\text{m}$  case. The maximum peaks of  $(v_{ix,z} - v_{xz})$  and  $(v_{gx,z} - v_{xz})$  are similar for both models.

The decoupling of the  $0.4\mu\text{m}$  grains is clearly seen in the ratio  $v_s/v_{gz}$  (equation (23)). Initially the grains are compressed along with  $\mathbf{B}$  and the ion fluid ( $v_s/v_{gz} \sim v_s/v_{iz}$ ) until after  $z \sim 3 \times 10^{16}\text{cm}$  when  $|\beta_g|$  and  $|Z_g|$  decrease. In which case, the grains are decoupled from  $\mathbf{B}$  and the compression slows compared with the ions. The grain fluid undergoes expansion until  $z = 3.7 \times 10^{16}\text{cm}$ . Compression then begins again, shown by increasing  $v_s/v_{gz}$ , with the transi-

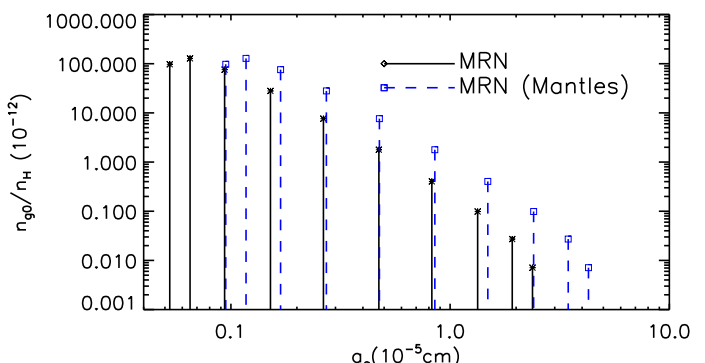


**Figure 4.** Grain radius  $a_g$  plotted with  $x_{g0} = n_{g0}/n_H$  for a standard MRN distribution (equation (60)) and a MRN distribution with grain coagulation and ice mantles using 10 grain size classes.

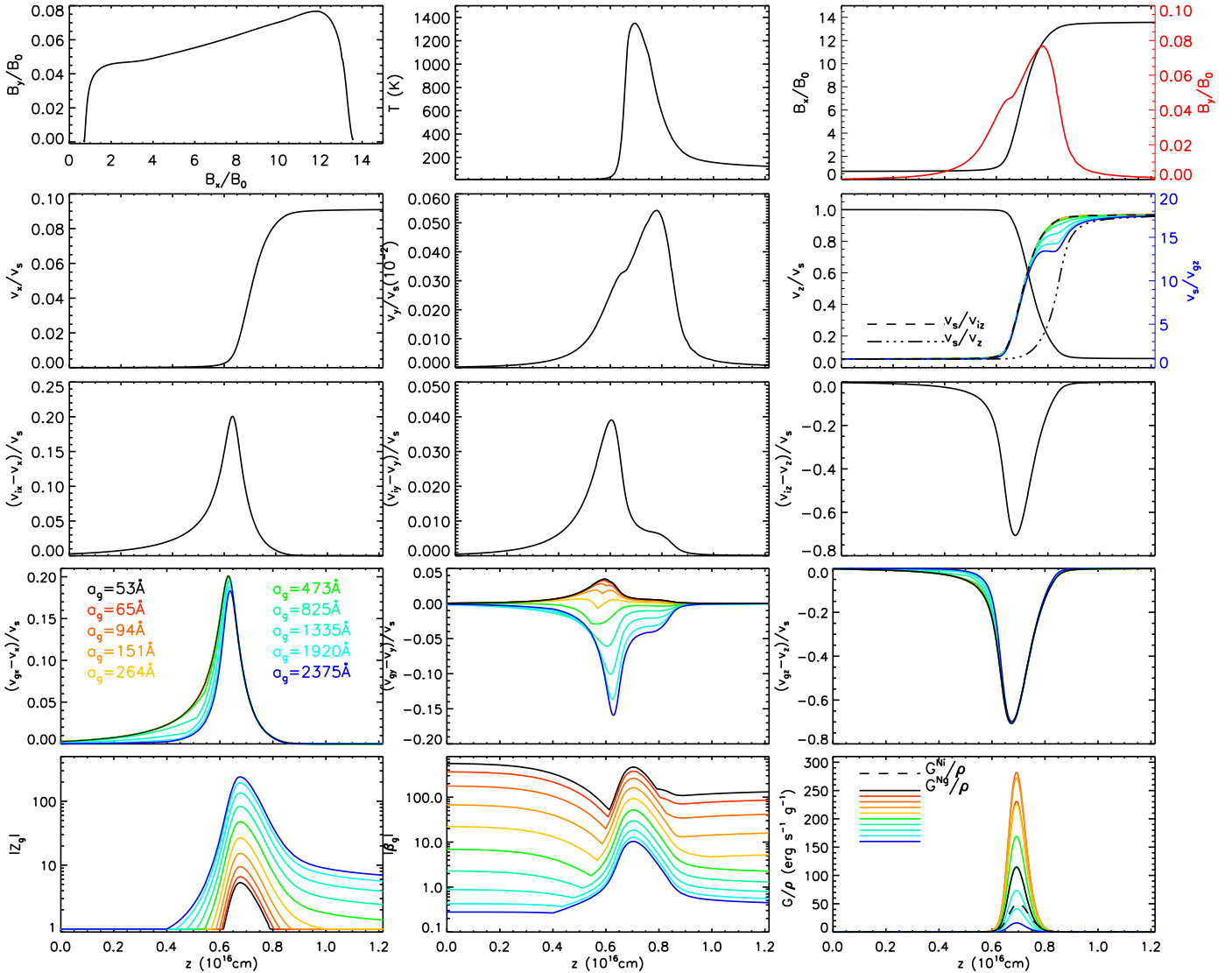


**Figure 5.** Shock profile with  $\theta = 45^\circ$  and the MRN grain size distribution of Fig. 4. The descriptions of the quantities are the same as for Fig. 1. The grain parameters for each size class are plotted in a different colour, with the radius  $a_g$  indicated in the  $(v_{gz} - v_z)$  plot.

tion of  $|\beta_g|$  from  $|\beta_g| > 1$  to  $|\beta_g| < 1$  as the grains become completely decoupled from  $\mathbf{B}$ , and compressed along with the neutrals after  $z = 3.7 \times 10^{16} \text{ cm}$ .

A lower grain abundance for the  $0.4\mu\text{m}$  model leads to a reduced heating rate per unit mass  $G^{ng}$ , whereas  $G^{ni}$  are similar for both models. The neutral temperature  $T$  (and  $T_{i,e}$ ), reaches smaller peak values, however the  $0.4\mu\text{m}$  grains obtain larger charge  $|Z_g(a_g, T_e)|$  as they have a larger surface area for electrons to stick to (equation (56)).

#### 9.4 MRN grain size distribution

In this section a MRN grain size distribution is adopted with 10 grain size classes.  $x_{g0} = n_{g0}/n_H$  versus size class  $a_g$ , (equation (60)) is plotted in Fig. 4 for the standard MRN grain size distribution. The total pre-shock grain density is  $\sum_g n_{g0} = 3.39 \times 10^{-5} \text{ cm}^{-3}$ , leading to  $x_{e0} = x_{i0} - \sum_g x_{g0} = 2.966 \times 10^{-8}$  (equation (14)). In general, the smaller  $a_g$ , the larger  $x_{g0}$ . The only exception is the  $65\text{\AA}$  class with  $x_{g0}$

greater than that of the  $53\text{\AA}$  class, since for smaller  $a_g$  the Gauss-Legendre weight  $w_m$  is less than the corresponding  $w_m$  for midrange  $a_g$  (equation (60)). A significant proportional (67%) of the total grain number density  $\sum_g n_{g0}$  comes from the smaller  $a_g \leq 65\text{\AA}$  grains, which couple best to the magnetic field and suppress  $\mathbf{B}$  diffusion. As the number of grain bins is increased from 1 to 10, the shock solution converges; The shock solution is already converged for  $> 10$  grain bins (plots not shown here).

Fig. 5 shows the corresponding shock profile. The maximum peak in  $B_y$  is significantly smaller than that of the equivalent  $0.1\mu\text{m}$  grain model (Fig. 2). The larger (low  $|\beta_g|$ ) size classes are better coupled to the neutrals through collisions, but their abundances are too low to have any large effect on the overall structure. The small dominant grain size classes (large  $|\beta_g|$ ) remain coupled to  $\mathbf{B}$  and so there is minimal rotation of  $\mathbf{B}$  out of the  $x-z$  plane, and subsequently a lower peak in  $B_y$ . The shock is also thinner and the peak in  $T$  is higher, compared with the single grain models.

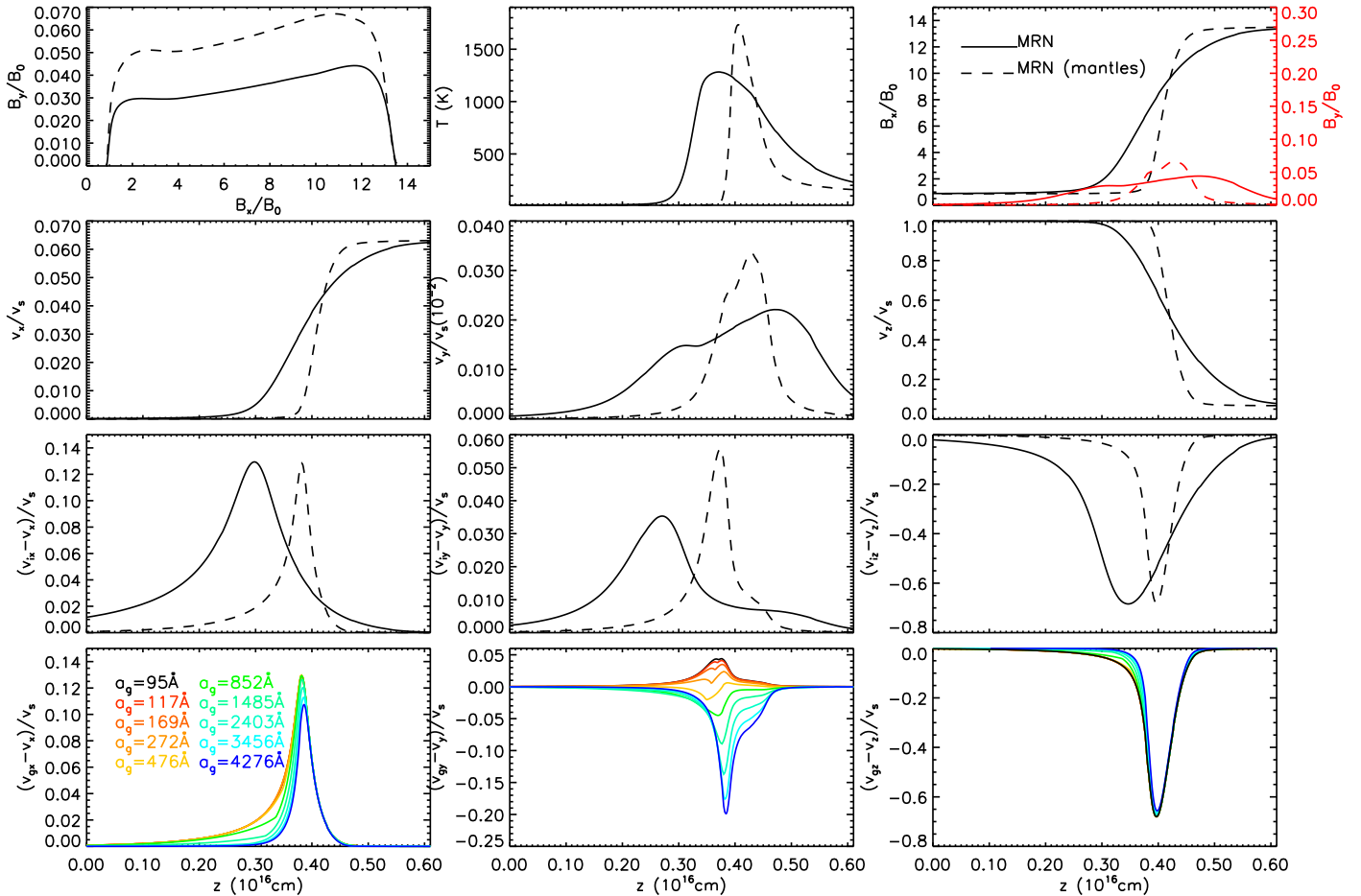


**Figure 6.** Shock profiles for the MRN grain size distribution (solid line) and MRN a distribution with mantles (dashed line), for  $\theta = 60^\circ$  and  $x_{g0}$  from Fig. 4.  $(v_{gx,y,z} - v_{x,y,z})$  are shown for the MRN(mantles) model only. The descriptions of the quantities are the same as in the caption for Fig. 5.

In Fig. 5,  $(v_{gx} - v_x)$  clearly differs with  $a_g$ , and the smallest grains are accelerated ahead of the larger grains until the peak at  $z = 0.63 \times 10^{16}$  cm. The  $|\beta_g|$  plot shows for the smallest grains  $|\beta_g| \gg 1$  through the entire shock with  $(v_{gx} - v_x) \sim (v_{ix} - v_x)$ . Conversely, for mid size range grains with  $|\beta_g| \ll 1$  initially,  $|\beta_g|$  reaches a maximum of only  $\sim 10$  due to increases in  $|Z_g|$ . The largest grains have the greatest surface areas, and so obtain largest  $|Z_g|$ . As  $|\beta_g|$  increases, the larger grains become better coupled to  $\mathbf{B}$  and  $(v_{gx} - v_x)_{large\ grain} \rightarrow (v_{gx} - v_x)_{small\ grain}$ . At  $z = 0.63 \times 10^{16}$  cm,  $(v_{gx} - v_x)$  is a maximum for all sizes, at which point  $v_x$  increases, and  $(v_{gx} - v_x)$  subsequently decreases, and all grain classes are (near) uniformly decelerated in  $x$  with respect to the neutrals. Similar comments can be made in regard to the magnitudes of  $(v_{gz} - v_z)$ .

$(v_{gy} - v_y)$  differ substantially with  $a_g$  in both sign and magnitude. The smallest  $a_g$  ( $|\beta_g| >> 1$ ) class have  $(v_{gy} - v_y) \sim (v_{iy} - v_y)$  as expected, and are accelerated ahead of the neutrals. However the largest  $a_g$  ( $|\beta_g| \sim 1-10$ ) class obtains large negative  $(v_{gy} - v_y)$  (as was also observed for the single  $0.4\mu\text{m}$  model). For each of the larger grains  $a_g \geq 825\text{\AA}$  there is a sharp trough in  $(v_{gy} - v_y)$  which coincides with  $|\beta_g| \sim 1$ , after which as  $|\beta_g|$  increases, the grains become better coupled to  $\mathbf{B}$  and  $|v_{gy} - v_y|$  decreases.

Each grain class is differentially compressed as shown in

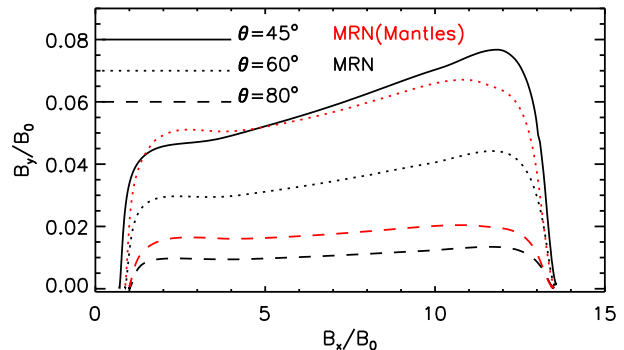


**Figure 7.**  $B_x - B_y$  phase plot for the MRN and MRN(Mantles) models, plotted in black and red respectively, and varying  $\theta = 45^\circ$  (solid),  $60^\circ$  (dotted), and  $80^\circ$  (dashed).

the  $v_s/v_{gz}$  plot (equation (23)) in Fig. 5. The compression of the larger  $a_g$  classes begins to slow ( $d(v_z^{-1})/dz \sim 0$ ) near  $z = 0.8 \times 10^{16}$  cm, before increasing as  $v_{gz} \rightarrow v_{zd}$ . Initially as  $|\beta_g|$  increases, the larger grain classes become better coupled to  $\mathbf{B}$  and are compressed along with the ions and  $\mathbf{B}$ . The compression then slows with decreasing  $|\beta_g|$  after  $z = 0.7 \times 10^{16}$  cm, and the larger grains decouple from  $\mathbf{B}$ . As  $\beta_g \approx 1$

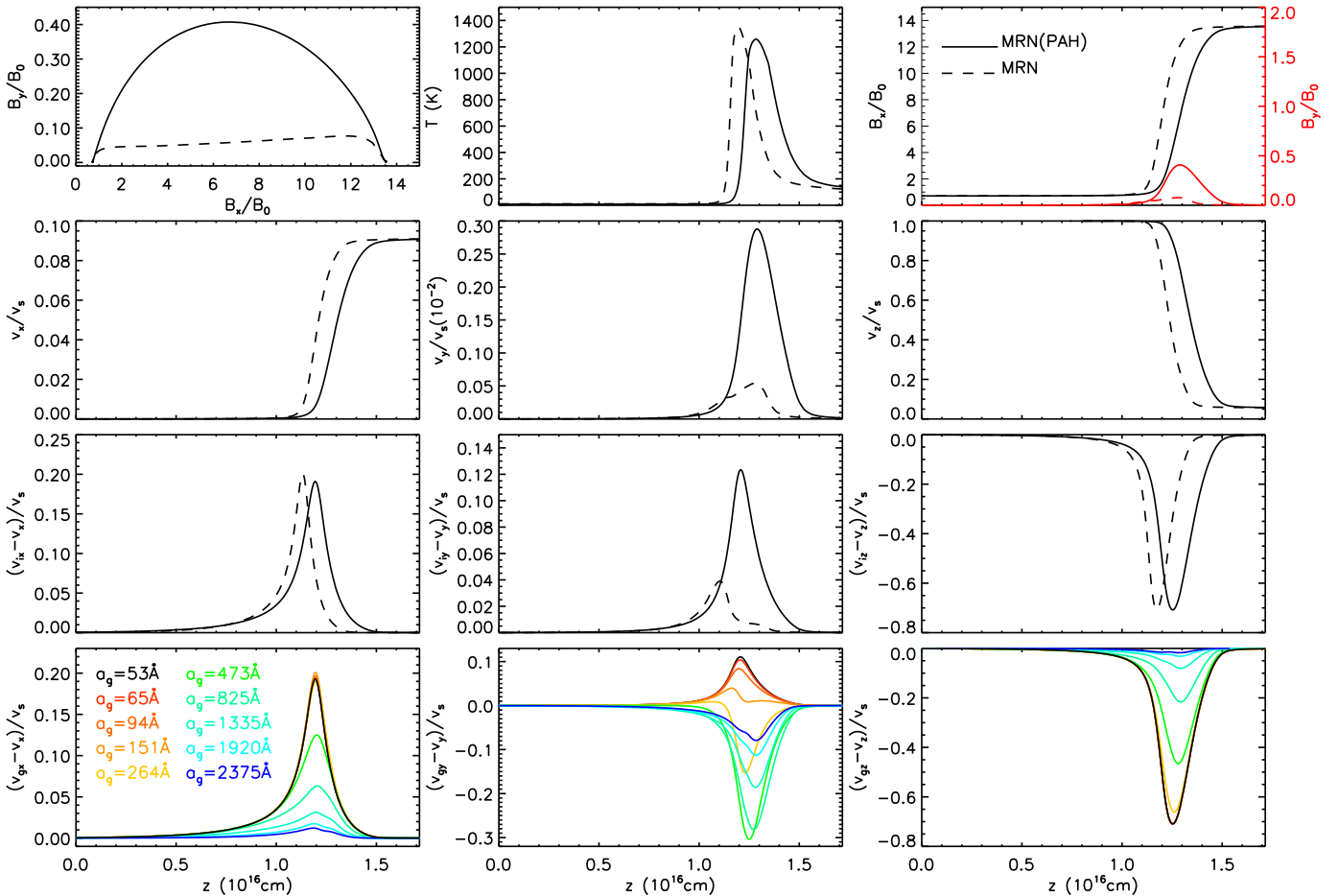


**Figure 8.** Shock profile for the MRN(PAH) model with  $\theta = 45^\circ$  (solid line). Also plotted is the MRN model from Fig. 5 (dashed line). ( $v_{gx,y,z} - v_{x,y,z}$ ) and  $v_s/v_{sz}$  are shown for the MRN(PAH) model only. The descriptions of the quantities are the same as in the caption for Fig. 5.

the compression slows  $(d(v_z^{-1})/dz \sim 0$  at  $z = 0.8 \times 10^{16}$  cm), after which  $|\beta_g|$  decreases further and the large grain classes are compressed along with the neutrals (see also Fig. 9.3). In general, the peak in  $G^{Ng}/\rho$ , also shown in Fig. 5, increase with decreasing  $a_g$  (due to increasing  $x_g$ ), and the smallest grains dominate the heating.  $G^{Ni}$  is comparable to that of the  $a_g = 1920\text{\AA}$  class.

### 9.5 MRN grain size distribution with mantles

The MRN distribution with ice mantles (discussed near equation (59)) is now considered.  $x_{g0}$  for each size class are shown in Fig. 4 with  $\sum_g n_{g0} = 3.39 \times 10^{-5} \text{ cm}^{-3}$ . A comparison of shock profiles for  $\theta = 60^\circ$ , using MRN distributions, with and without grain mantles are shown in Fig. 6. The rotation of  $\mathbf{B}_\perp$  is increased for the MRN(mantles) case as the grain size classes are larger and are only partially coupled to  $\mathbf{B}$ . The shock width is narrower with a corresponding higher peak  $T$ . A higher peak in  $T$  leads to higher  $c_s$ , and shock solutions are limited to  $\theta_{crit} \sim 60^\circ$  for the MRN(mantles) model, as opposed to  $\theta_{crit} \sim 45^\circ$  for the MRN case. A larger peak in  $B_y$  leads to higher peaks in  $v_y$  and  $(v_{iy} - v_y)$ .  $(v_{ix,z} - v_{x,z})$  and  $v_{x,z}$  are similar in magnitude for both models. In general the grain drift velocities show similar trends to the MRN model (Fig. 5).

The  $B_x - B_y$  phase plots for the MRN and MRN(mantles) models with varying  $\theta$  are compared in Fig. 7. In general, there is a decrease in the rotation of  $\mathbf{B}_\perp$  with increasing  $\theta$ . The corresponding effects on the neutral and charged species dynamics follow on from the relative magnitude of  $B_y$  through the shock. MRN(mantles)  $\theta = 60^\circ$  is essentially equivalent to MRN  $\theta = 45^\circ$ . Increasing the grain sizes, which leads to larger forces out of the shock plane and a more non-coplanar solution, is essentially equivalent to taking a MRN distribution with smaller  $\theta$ . This result is initially surprising as one might expect the addition of more highly coupled charge carriers with  $|\beta_g| >> 1$  to reduce the Hall current. However electron abundance and therefore net charging of grains is reduced, so many grains remain decoupled from  $\mathbf{B}$ .

### 9.6 MRN with PAHs

In the interstellar medium, for  $n_H = 10^5 \text{ cm}^{-3}$ , the abundance of negatively charged PAHs<sup>-</sup> is of the order  $10^{-8}$ , with a similar total abundance,  $1.1 \times 10^{-8}$ , of ions and positively charged PAH<sup>+</sup>s (values taken from Fig. 1 of Kaufman & Neufeld (1996)). Assuming a MRN distribution as before,  $\sum_g x_{g0} = 3.39 \times 10^{-10}$ , a PAH<sup>-</sup> component;

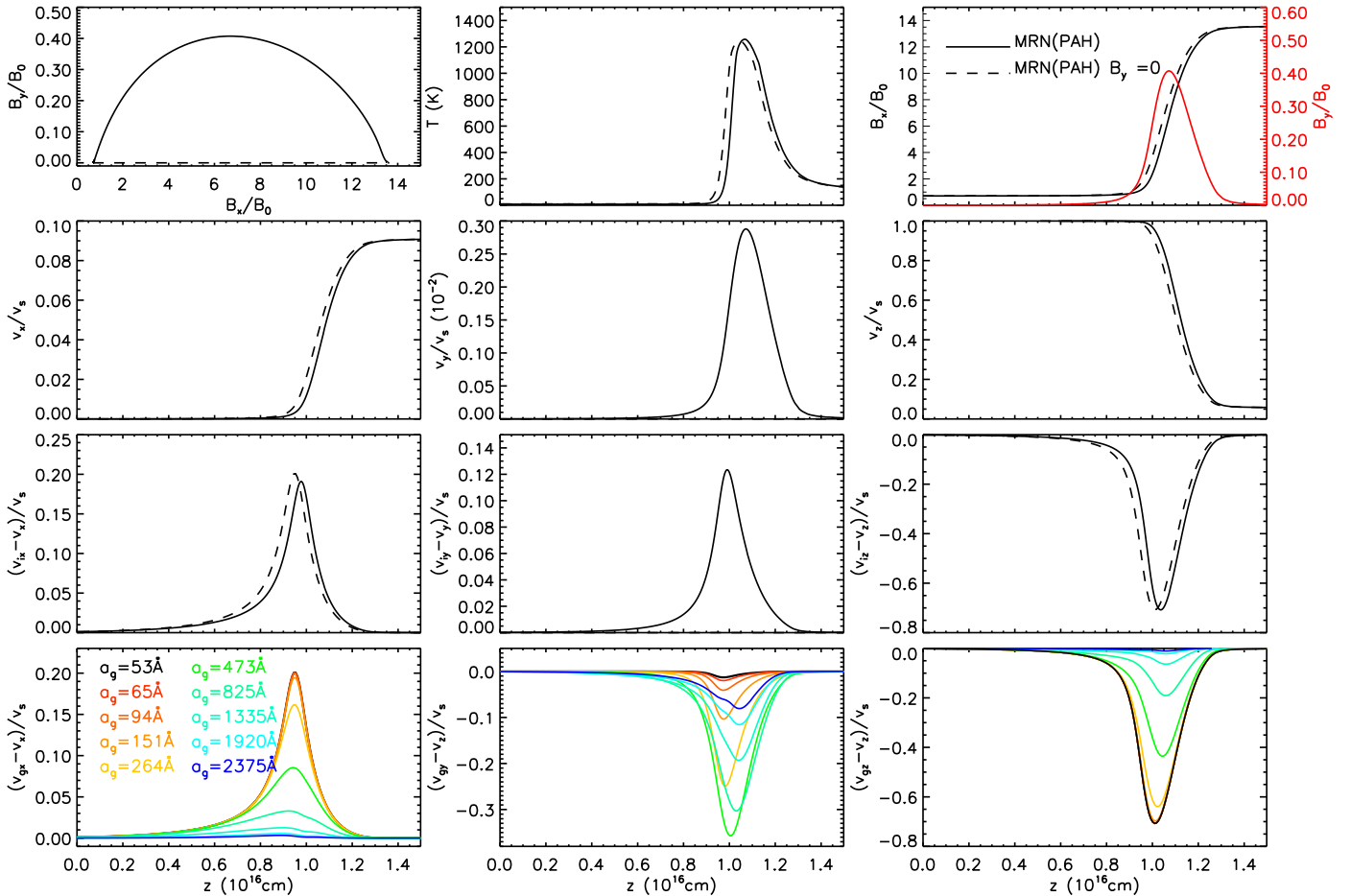


**Figure 9.** Shock profile for MRN(PAH) model  $B_y = 0$  (dashed) and  $\theta = 45^\circ$ . The solid line is the MRN(PAH) model (Fig. 8).  $(v_{gx,y,z} - v_{x,y,z})$  are shown for the MRN(PAH)  $B_y = 0$  model only.

$x_{pah0} = 1 \times 10^{-8}$ , and the corresponding PAH<sup>+</sup> and ion component;  $x_{i0} = 1.1 \times 10^{-8}$ , then by charge neutrality,  $x_{e0} = 6.606 \times 10^{-10}$  (consistent with  $x_{e0}$  in Kaufman & Neufeld (1996)). Since  $x_{e0}$  is two orders of magnitude lower than in the previous models (Sections 9.1–9.5), there are not enough electrons to charge all grain classes inside the shock. Even if only the smaller grain size classes are charged, which account for a significant fraction of the total grain surface area, these are already highly coupled to  $\mathbf{B}$  ( $|\beta_g| \gg 1$ ) and increasing  $|Z_g|$  does not effect the grain dynamics or the shock structure. For simplicity,  $Z_g$  is assumed constant ( $Z_g = -1$ ). The rate coefficient for PAH-neutral scattering is the same as for the ions with  $\langle \sigma v \rangle_{pah} = 1.6 \times 10^{-9} \text{ cm}^3 \text{s}^{-1}$  (Wardle 1998), and  $\beta_{pah0} = -\beta_{i0} = -1.382 \times 10^4$ .

The shock profiles ( $\theta = 45^\circ$ ) for MRN(PAH) and MRN are compared in Fig. 8. There is significantly more  $\mathbf{B}_\perp$  rotation for the MRN(PAH) model. The  $B_x$  and  $T$  profiles are similar, leading to the close similarities in  $v_x$  ( $v_{ix} - v_x$ ) and  $v_z$  ( $v_{iz} - v_z$ ). Ions, electrons, and PAHs, remain well coupled to  $\mathbf{B}$ , and  $(\mathbf{v}_i - \mathbf{v}) = (\mathbf{v}_{pah} - \mathbf{v})$ .

There is a clear distinction between  $(v_{gx,z} - v_{x,z})$  for the smaller and larger grain classes. The smaller grains remain well coupled to  $\mathbf{B}$ , whereas, the larger grains remain highly coupled to the neutrals through collisions and are co-moving with them ( $v_{gx,z} - v_{x,z} \sim 0$ ). With fixed  $Z_g$ , the larger grains do not become increasingly coupled to  $\mathbf{B}$  as

they pass through the shock (as in the previous results for MRN). From upstream to downstream, each smaller grain is compressed ahead of the next larger grain. The smallest grains are compressed with the ions and magnetic field through the entire shock, and the larger grains are compressed with the neutrals. The midrange size class ratios  $v_s/v_{zg}$  lie between these two extremes.

$(v_{gy} - v_y)$  show (in general) similar relationships between the relative magnitude and sign with grain class size, as seen previously in Fig. 5. Smaller grain classes are coupled to  $\mathbf{B}$  with  $(v_{gy} - v_y) \sim (v_{iy} - v_y) > 0$ , and the larger grain classes have  $(v_{gy} - v_y) < 0$ . There is also a turnover in the magnitude of  $(v_{gy} - v_y)$  with increasing  $a_g$ . The larger grain size classes ( $|\beta_g| \ll 1$ ) are highly coupled to the neutrals and have small  $|v_{gy} - v_y|$ . As  $a_g$  decreases ( $|\beta_g| \sim 1-10$ ), Hall effects are present and these obtain larger negative  $(v_{gy} - v_y)$ . As  $a_g$  is decreased further, the coupling to  $\mathbf{B}$  increases, and  $(v_{gy} - v_y) \rightarrow (v_{iy} - v_y)$ .

## 9.7 Suppressing $B_y$

Fig. 9 shows the effect of suppressing  $B_y$  in the MRN(PAH) model.  $v_{x,y,z}$ ,  $(v_{gx,z} - v_{x,z})$  and  $(v_{ix,z} - v_{x,z})$  are essentially unaltered, except for the slightly higher peak in  $(v_{ix} - v_x)$  for  $B_y = 0$ , due to the corresponding differences in  $(\mathbf{E}' \times \mathbf{B})_x$ .

The peak in  $T$  is lower for  $B_y = 0$ , but only by  $\sim 10\text{K}$ . The heating rate is increased, however the cooling rate is a strong function of  $T$  and so the change in  $T$  is small. In  $y$  all grain size classes lag the neutrals ( $v_{gy} - v_y < 0$ ), and for the smallest grains ( $v_{gy} - v_y \sim 0$ ). The larger grain size classes have similar ( $v_{gy} - v_y$ ) as in Fig. 8 as they are decoupled from  $\mathbf{B}$ , and so are unaffected by changes in  $B_y$ . The corresponding  $B_y = 0$  results of the models in Sections 9.1-9.6 plots not shown) also show only minor differences.

## 10 DISCUSSION

The results above demonstrate the effects of charged dust grains on the structure of fast C-type shocks. For  $n_H = 10^5\text{cm}^{-3}$  and shock speed  $v_s = 18\text{km/s}$  radiative C-type shock solutions exist ( $\theta_{critical} < \theta < 90^\circ$ ). The grain model details, i.e., modelling the grain population as either a separate grain species or else as a continuous grain size distribution, is important to the overall shock structure, as well as the dynamics of the individual grain species/size classes.

The grain models considered here were chosen to illustrate the main qualitative changes in the resulting shocks. The shock profiles were clearly altered with the introduction of a grain size distribution as opposed to the single sized grain models. The net charge on the grains is increased for the MRN models with the grains becoming better coupled to the magnetic field, resulting in less magnetic field rotation inside the shock front. The MRN(mantles) and MRN(PAH) models were chosen to illustrate changes in the shock profiles when departing from the standard MRN model. It should be noted that the MRN(mantles) model is not purely a MRN model with growth of ice mantles of constant thickness. We have followed the model of Nishi, Nakano & Umebayashi (1991) who increase the size of the grains by a factor of 9/5. The qualitative changes are clear though; any increase in the grain sizes leading to larger grain surface areas (larger grain charge) will cause an increase in the net charge on the grains, and the grain coupling to  $\mathbf{B}$ . However, by increasing the collisional cross section, the grains are increasingly coupled to the neutrals via collisions. In the MRN(mantles) models shown in section 9.5, the latter effect was dominant with the MRN(mantles) solution showing more magnetic field rotation than its MRN counterpart.

As  $\mathbf{B}$  is compressed inside the shock, the charged species are accelerated with respect to the neutrals, however, this is opposed by the collisional drag of the neutrals. If the grains are highly coupled to  $\mathbf{B}$  (high  $|\beta_g|$ ) and the movements of the neutrals and other highly coupled species (i.e., ions, PAHs, and electrons) are mainly restricted to the  $x-z$  plane, then  $B_y$  is small. If however, the grains are only partially coupled to  $\mathbf{B}$ , either because they are large in size and so are better coupled to the neutral fluid via collisions and/or have low charge  $|Z_g|$  (and low  $|\beta_g|$ ), then the grains drift out of the  $x-z$  plane, and the shock becomes non-coplanar with large  $B_y$ . The grains dominate the collisional heating of the neutrals, with only a small contribution from the ions and a negligible component from the electrons (due to their low mass).

The non-coplanarity in the shock solution depends on the grain model; the single grain models (Sections 9.1-9.3) produce significantly more rotation of  $\mathbf{B}_\perp$  than for the MRN models (Sections 9.4-9.6). For both  $0.1\mu\text{m}$  and  $0.4\mu\text{m}$

models, the grains were only partially coupled to  $\mathbf{B}$  with  $|\beta_g| \sim 0.1 - 10$  inside the shock and the out-of-plane forces are substantial. For the MRN models, rotation of  $\mathbf{B}$  is minimal, since the more abundant, smaller  $a_g$  classes ( $|\beta_g| >> 1$ ) which are highly coupled to  $\mathbf{B}$ , dominate the net grain effects on the shock structure.

As  $\theta \rightarrow 90^\circ$  the peak in  $B_y$  decreases, for a given grain model, and the well  $\mathbf{B}$  coupled charged species are restricted to the shock plane (weakly coupled grains are still able to drift out of the shock plane).  $\mathbf{B}_\perp$  rotation increases with decreasing  $\theta$  and  $|\mathbf{v}_j - \mathbf{v}|$  become larger (on average), resulting in more dissipation. The shock must dissipate the incoming kinetic energy flux over a shorter length scale, and the peak temperature  $T$  inside low  $\theta$  shocks (for a given grain size model) are therefore higher than for high  $\theta$  shocks. For low  $\theta$  shocks, the neutral fluid experiences more compression as it cools and so the sound speed is higher in the final part of the flow. There is a critical point for low enough  $\theta$ , that in the neutral fluid  $v_z = c_s$ , in which case the derivative  $dP/dz$  is ill-defined (equation (28)) and the shock solution is no longer C-type. Below this critical angle  $\theta < \theta_{critical}$  the shock solutions may be either J-type or C\*-type. The limiting value of  $\theta_{critical}$  varied with grain model, but the ordering remains same, the higher the peak temperature in the shock, the larger  $\theta_{critical}$ .

Grains dominate the collisional heating of the neutrals. The peak  $T$  was higher and shock width narrower for the  $0.1\mu\text{m}$  model (Section 9.1) compared with the  $0.4\mu\text{m}$  model (Section 9.3) since the pre-shock abundance of the  $0.1\mu\text{m}$  grains was two orders of magnitude larger, than for the  $0.4\mu\text{m}$  model, which compensated for their smaller collisional cross-sections. Conversely, for the MRN(mantles) model (Section 9.5), the increase in the total frictional heating of the neutrals due to the increase in the net grain collisional cross-sections lead to hotter thinner shocks than for the MRN model with an equivalent pre-shock grain abundance (Section 9.4). Since the temperatures, and subsequently  $c_s$ , are higher in the MRN(mantles) model (for a given  $\theta$ ), it is more difficult for the neutral fluid to maintain supersonic flow and subsequently  $\theta$  is restricted to  $\theta > \theta_{critical} \sim 60^\circ$  for the MRN(mantles) model but only  $\theta > \theta_{critical} \sim 45^\circ$  for the MRN model (for  $v_s$  and  $n_H$  considered here).

There are also critical values of  $n_H$  for which C-type solutions do not exist. Increasing  $n_H$  (for a given  $\theta$ ), increases the neutral-grain collisional heating rates and thus dissipation. With a large enough increase in  $T$  and  $c_s$  the neutral flow cannot remain supersonic. For all grain models considered here, the C-type solutions also broke down for  $n_H > 10^5\text{cm}^{-3}$  (independent of  $\theta$ ), with only J-type or C\*-type shocks possible. The exact limits of  $\theta$  and  $n_H$  could vary with the choice of cooling function. The Lepp & Shull (1983) cooling rate has been used here, other treatments of the cooling rate (Martin, Schwart & Mandy 1996; Galli & Palla 1998), will lead to different temperature structures and thus different limits on  $\theta$  and  $n_H$ . However the orderings of the different grain models will remain the same; the cooler MRN and  $0.4\mu\text{m}$  models will have lower  $\theta_{critical}$  than the hotter MRN(mantles) and  $0.1\mu\text{m}$  models, respectively.

In the MRN models (Sections 9.4-9.5) the  $T_e$  dependent grain charging,  $Z_g(T_e)$ , increased the grain coupling to  $\mathbf{B}$ . The smaller  $a_g$  classes  $|\beta_g| >> 1$  were compressed with

the ion fluid and  $\mathbf{B}$ . Mid range grains remained coupled to  $\mathbf{B}$  until reductions in  $Z_g$  lead to their decoupling from  $\mathbf{B}$ , and were compressed with the neutral fluid thereafter. The largest grains  $|\beta_g| \ll 1$  are essentially compressed along with the neutral fluid. When PAHs are present (Section 9.6),  $x_{e0}$  is reduced with  $Z_g = -1$ , and the mid to large grain size classes are less coupled to  $\mathbf{B}$  and are (on average) decoupled further by neutral collisions inside the shock. As a result there is a larger Hall current and the amount of rotation of  $\mathbf{B}_\perp$  is increased.

Here  $T_e$  is given by the approximation in equation (55) based upon Fig. 1 of Draine et al. (1983). Changing the treatment of  $T_e$  could largely effect  $Z_g$  of the larger grains and alter their coupling to  $\mathbf{B}$  as well as  $(\mathbf{v}_g - \mathbf{v})$ . However, smaller grains with low  $Z_g$  are highly coupled to  $\mathbf{B}$  (essentially independent of  $T_e$  and  $Z_g$ ) and dominate the grain effects on shock structure. Thus variations in the treatment of  $T_e$  are unlikely to change the model results.

$|Z_g|$  increases with increasing  $T_e$  according to equation (56), however as  $T_e$  decreases, the uncharging proceeds simply via the re-release of the captured electrons. More realistically the reduction in  $|Z_g|$  proceeds via the capture of ions (Draine & Sutin 1987), and the ion fluid is depleted. Moreover, inside shock waves in dense clouds, negatively charged PAHs may be neutralized in neutral-PAH<sup>-</sup> reactions, resulting in electron detachment (Pineau des Forets et al. 1988). Flower & Pineau des Forets (2003) modelled the charge variations of grains in a planar steady C-type shock with  $v_s = 50\text{km/s}$ . The grain population was represented by a small (dominant) PAH grain component and a large grain component (given by an MRN distribution  $0.01 \leq a_g \leq 0.3\mu\text{m}$ ), and they found that the charge variations for each were very different. The PAHs were neutralised by neutral-PAH<sup>-</sup> reactions via electron detachment, while the larger grains became more negatively charged as  $T_e$  and thus  $|Z_g|$  increased through the shock.

Detachment of electrons via neutralization of the PAH<sup>-</sup>s, may allow for the  $Z_g(a, T_e)$  (equation (56)) charging to proceed in the MRN(PAH) model, potentially increasing the grain- $\mathbf{B}$  coupling, reducing the rotation of  $\mathbf{B}_\perp$ . However, the capture of ions could also counteract any increases in  $Z_g$ . The shock model of Flower & Pineau des Forets (2003), included both electron and ion attachment on the grain surfaces, and the net negative charge on the grain component still increased significantly due to the increase in the attachment rate of electrons with increasing  $T_e$ . Thus, it is likely that if ion attachment were included in the models here,  $|Z_g|$  should still increase with  $T_e$ . The details of this will need to be quantified and confirmed in further studies.

Inertia of the grains has also been neglected and their drift is given by the balance of electromagnetic forces and neutral-grain collisional drag. Ciolek & Roberge (2002) demonstrated that for very small grains ( $a_g < 0.1\mu\text{m}$ ) the length scales over which the neutral fluid and magnetic field were compressed,  $L_{neut}$  and  $L_{field}$ , respectively, are over three orders of magnitude larger than the length scales for the gas drag to decelerate the grains  $L_{drag}(g)$ . Thus, neglecting the inertia of the smaller grains is a good approximation. However, for the large grains ( $a_g \gtrsim 0.1\mu\text{m}$ ),  $L_{drag}(g)$  is of the same order as  $L_{field}$  and so the inertia cannot be neglected. The larger grains dominate the field-neutral coupling and so the inclusion of their inertia may effect the shock structure.

The amount of dissipation inside the shock was relatively insensitive to the orientation of  $\mathbf{B}_0$  for the pre-shock conditions considered here;  $n_H = 10^5\text{cm}^{-3}$ . The peak  $T$  inside the shock was essentially unaltered when  $B_y = 0$  for the MRN(PAH) model (Section 9.7) even though the MRN(PAH) model had the most  $\mathbf{B}_\perp$  rotation. Similar comparisons have been made for the other MRN models. The critical angle  $\theta_{critical}$  for which the neutral flow inside the shock makes the transition from supersonic to subsonic is also unaltered when  $B_y$  is suppressed. For the purposes of calculating detailed chemical models and molecular line emission the shock problem can be greatly simplified by suppressing  $B_y$ . This may not be the case, however, for higher  $n_H$  where grains may become further decoupled from  $\mathbf{B}$ .

The choice of grain model affects the shock structure, however, the same overall jump conditions (for given pre-shock conditions) are still satisfied, and the same power per unit area is dissipated inside the layer of hot gas inside the shock transition. For the models here, the temperatures inside the shock reach  $\sim 1500\text{K}$  and the molecules will remain intact, so the molecular line emission should be similar regardless of the grain model. Neufeld & Stone (1997) numerically modelled CO and H<sub>2</sub> line emission for C-type shocks subject to the Wardle instability, concluding that the line strengths are relatively insensitive to the exact details of the shock structure. However, the choice of grain model does effect the limits  $n_H$  and  $\theta$  for which the shock becomes J-type (or C\* type), and the temperatures inside J-type shock reach much higher values, so the shocked molecules may not always remain intact.

## 11 SUMMARY

New shock models for fast oblique C-type shocks have been presented here with pre-shock conditions  $n_H = 10^5\text{cm}^{-3}$ ,  $v_s = 18\text{km/s}$ , and  $M_A = 10$  for freely specified magnetic field  $\mathbf{B}_0$  orientation  $35^\circ \leq \theta \leq 80^\circ$ . The grain population is represented by either

- a single grain population of size  $0.1\mu\text{m}$  or  $0.4\mu\text{m}$ ,
- a continuous (standard) MRN grain size distribution,
- a MRN distribution with ice mantles, or
- a MRN distribution with additional populations of positively and negatively charged PAHs.

There were clear differences in the shock profiles with grain model due to the coupling of the grains to either/both the magnetic field and/or neutral fluid. Smaller and/or highly charged grains remain well coupled to  $\mathbf{B}$  whereas larger grains are coupled to the neutral fluid through collisions. Shock models with grain populations that are well coupled to  $\mathbf{B}$  result in more co-planar shock profiles with minimal rotation of  $\mathbf{B}$  out of the shock plane. The results are summarized below:

- For a given  $\theta$ , the smaller  $0.1\mu\text{m}$  grain model produces more co-planar solutions than the  $0.4\mu\text{m}$  model since the  $0.1\mu\text{m}$  grains are better coupled to  $\mathbf{B}$ .
- Each grain size class in the MRN models were differentially accelerated inside the shock front, with the largest grains being compressed along with the neutrals and the smaller grains compressed along with the ions and  $\mathbf{B}$ .

- The more abundant, smaller grains in the MRN distribution models dominate the net grain effects on the shock structure resulting in more co-planar solutions compared with the single grain models.
- The effect of charging grains via the capture of the electrons increased the grain- $\mathbf{B}$  coupling in all grain models.
- The increase in the grain surface areas from the MRN to the MRN(mantles) models increased the net grain charge, however the increase in the grain collisional cross sections resulted in better coupling of the grains to the neutrals and consequently more rotation of  $\mathbf{B}$  out of the shock plane, for a given  $\theta$ .
- The grains dominate the drag force and collisional heating of the neutrals, so the models with larger (larger collisional cross sections) or more abundant grains have higher peak temperatures and the shock fronts are subsequently narrower i.e., the collisional heating for the less abundant  $0.4\mu\text{m}$  grains lead to lower peak shock temperatures and wider shock fronts than for the more abundant  $0.1\mu\text{m}$  grains. Conversely, the larger MRN(mantles) model lead to increased peak temperatures, and narrower shock fronts, compared with the MRN model, due to the increase in the collisional cross section of the grains.
- The higher the peak temperatures reached inside the shock front, the higher the sound speed and the neutrals cannot always remain supersonic. As a result, the lower limit of  $\theta$  for which C-type solutions are possible is dependent on grain model;  $\theta_{\text{critical}} \sim 40^\circ$  for the  $0.1\mu\text{m}$  model,  $\theta_{\text{critical}} \sim 45^\circ$  for the MRN and MRN(PAHs) models,  $\theta_{\text{critical}} \sim 60^\circ$  for the MRN(mantles) model (for  $v_s$  and  $n_H$  considered here).
- The non-coplanarity of the shock solution is also dependent upon the orientation of  $\mathbf{B}_0$ , with the peak in  $B_y$  decreasing as  $\theta \rightarrow 90^\circ$ .
- For pre-shock conditions considered here ( $n_H = 10^5\text{cm}^{-3}$ ,  $v_s = 18\text{km/s}$ ) the amount of dissipation inside the shock is relatively insensitive to the orientation of  $\mathbf{B}_0$ , so in calculating molecular line emission or chemical models the shock problem is greatly simplified by suppressing  $B_y$ .

## ACKNOWLEDGMENTS

This research was supported by the Australian Research Council.

## REFERENCES

- Carrasco L., Strom S.E., Strom K.M., 1973, ApJ, 182, 95  
 Chernoff D.F., 1987, ApJ, 312, 143  
 Chernoff D.F., McKee C.F., Hollenbach D.J., 1982, ApJ, 259, L97  
 Chokshi A., Tielens A.G.G.M., Hollenbach D., 1993, ApJ, 407, 806  
 Ciolek G.E., Roberge W.G., 2002, ApJ, 567, 947  
 Cowling T.G., 1976, Magnetohydrodynamics, 2nd edn.  
 Hilger, London  
 Draine B.T., 1980, ApJ, 241, 1021  
 Draine B.T., 1986, MNRAS, 220, 133  
 Draine B.T., Katz N., 1986a, ApJ, 306, 655  
 Draine B.T., Katz N., 1986b, ApJ, 310, 392  
 Draine B.T., Lee H.M., 1984, ApJ, 285, 89  
 Draine B.T., Roberge W.G., 1982, ApJ, 259, L91  
 Draine B.T., Roberge W.G., Dalgarno A., 1983, ApJ, 264, 485  
 Draine B.T., Sutin B., 1987 ApJ, 320, 803  
 Elmegreen B.G., 1979, ApJ, 232, 729  
 Flower, D.R., Pineau des Forêts G., 2003, MNRAS, 343, 390  
 Flower D.R., Pineau des Forêts G., Hartquist T.W., 1985, MNRAS, 216, 775  
 Gail H.P., Sedlmayr E., 1975, ApJ, 41, 359  
 Galli D., Palla F., 1998, A&A, 335, 403  
 Gear C.W., 1971, Numerical value problems in ordinary differential equations. Prentice Hall, Eaglewood Cliffs  
 Goldsmith P.F., Langer W.D., 1978, ApJ, 222, 881  
 Hartquist T.W., Caselli P., 1998, The molecular astrophysics of stars and galaxies. Clarendon Press Oxford, 179  
 Kaufman M.J., Neufeld D.A., 1996, ApJ, 456, 250  
 Lepp S., Shull J.M., 1980, ApJ, 270, 578  
 Li, A., Greenberg J.M., 2003, in Solid State Astrochemistry, ed. V. Pirronello, J. Krelowski, & G. Manicó, (Dordrecht: Kluwer), 37  
 Martin P.G., Schwart D.H., Mandy M.E., 1996, ApJ, 461, 265  
 Mathis J.S., Rumpl W., Nordsieck K.H., 1977, ApJ, 217, 425  
 McCray R., Snow T.P., 1979, ARA&A, 17, 213  
 Mullan D.J., 1971, MNRAS, 153, 145  
 Nishi R., Nakano T., Umebayashi, T., 1991, ApJ, 368, 181  
 Neufeld D.A., Stone J.M., 1997, ApJ, 487, 283  
 Pilipp W., Harquist T.W., 1994, MNRAS, 267, 801  
 Pineau des Forêts G., Flower D.R., Dalgarno A., 1988, MNRAS, 235, 621  
 Pineau des Forêts G., Flower D.R., Hartquist, T.W., Dalgarno A., 1986, MNRAS, 220, 801  
 Press W.H., Teukolsky S.A., Vetterling W.T., Flannery B.P., 1992, Numerical recipes in FORTRAN: The art of scientific computing 2nd edn. Cambridge Univ. Press, Cambridge  
 Roberge W.G., Draine B.T., 1990, ApJ, 350, 700  
 Shu F.H., 1983, ApJ, 273, 202  
 Spitzer L., 1978, Physical processes in the interstellar medium. New York Wiley-Interscience, 333  
 Wardle M., 1991, MNRAS, 251, 119  
 Wardle M., 1998, MNRAS, 298, 507  
 Wardle M., Draine B.T., 1987, ApJ, 321, 321  
 Wardle M., Ng C., 1999, MNRAS, 303, 239  
 Weingartner J.C., Draine B.T., 2001, ApJ, 548, 296  
 Whittet D.C.B., Bode M.F., Longmore A.J., Baines D.W.T., Evans A., 1983, Nat, 303, 218